



GEORG-AUGUST-UNIVERSITÄT  
GÖTTINGEN



## **Bachelor's Thesis**

# **Constraining Exoplanet Characteristics with Asteroseismology**

## **Einschränkung der Eigenschaften extrasolarer Planeten mittels Asteroseismologie**

prepared by

**Tim Lichtenberg**

from München

at the Institut für Astrophysik

**Thesis period:** 14th May 2012 until 20th August 2012

**First referee:** Prof. Dr. Laurent Gizon

**Second referee:** Prof. Dr. Stefan Dreizler



## Abstract

In this thesis I study the precision of exoplanetary characteristics, in particular their masses and radii, by using different methods. I highlight the supposed improvements provided by asteroseismic studies.

To calculate the exoplanetary parameters, I use five different calculation methods for the model systems Kepler-10, 21 and 22. The distinctions are set in the computation of the required stellar parameters.

I show that the precision increases with the use of asteroseismology, though only asteroseismic modeling improves the exoplanet parameters significantly. Other methods used in this thesis refine the accuracy only under certain conditions.

At last I give a short prospect on future possibilities with planned space missions.

## Zusammenfassung

Diese Bachelorarbeit befasst sich mit der Präzision der Parameterbestimmung von extrasolaren Planeten bei Nutzung unterschiedlicher Herangehensweisen. Ein besonderer Fokus wird dabei auf die gemutmaßten Verbesserungen durch Asteroseismologie gelegt.

Es werden fünf unterschiedliche numerische Berechnungen durchgeführt, um einige Eigenschaften, insbesondere die Masse und den Radius, der drei Modellsysteme Kepler-10, 21 und 22 zu bestimmen. Die Unterschiede liegen dabei in der Berechnung der dafür nötigen Sternparameter.

Es kann gezeigt werden, dass die Genauigkeit durch Asteroseismologie grundsätzlich gesteigert werden kann, ein wirklich nutzbringender Effekt aber erst mit durchgeführter Modellierung zu erkennen ist. Die in dieser Arbeit genutzte Methode bringt nur unter gewissen Umständen Vorteile.

Zum Schluss wird noch ein Ausblick auf zukünftige Möglichkeiten mit voll gegebener asteroseismischer Präzision gegeben.



# Contents

<b>1. Introduction</b>	<b>1</b>
<b>2. Observing and modeling stars</b>	<b>3</b>
2.1. Classical observations . . . . .	3
2.1.1. Astrometry . . . . .	3
2.1.2. Photometry and Spectroscopy . . . . .	3
2.2. Asteroseismology of solar-like stars . . . . .	5
2.2.1. Introduction . . . . .	5
2.2.2. Basic properties of stellar oscillations . . . . .	5
2.2.3. Other types of stellar oscillations . . . . .	9
2.2.4. Interpretation of stellar oscillation frequencies . . . . .	9
2.2.5. Classical vs. asteroseismic stellar modeling . . . . .	10
<b>3. Detecting and characterizing exoplanets</b>	<b>13</b>
3.1. Detection methods . . . . .	13
3.1.1. Transit events . . . . .	13
3.1.2. Doppler spectroscopy . . . . .	15
3.1.3. Other methods . . . . .	16
3.2. Describing exoplanetary orbits . . . . .	17
3.2.1. Inferences from transit light curves . . . . .	17
3.2.2. Combining transit and radial velocity measurements . . . . .	19
3.2.3. Habitability of exoplanets . . . . .	19
3.3. Exoplanet detection programmes . . . . .	20
3.3.1. Radial velocity instruments . . . . .	20
3.3.2. Transit searches from space . . . . .	21
3.3.3. Future observations . . . . .	21

<b>4. Numerical experiment</b>	<b>23</b>
4.1. Analyzed exoplanet systems . . . . .	23
4.1.1. Kepler-21 . . . . .	23
4.1.2. Kepler-10 and Kepler-22 . . . . .	24
4.2. Methods of the parameter study . . . . .	28
4.2.1. Stellar parameters . . . . .	28
4.2.2. Exoplanet characteristics . . . . .	30
<b>5. Results and discussion</b>	<b>33</b>
5.1. Validation and systematics . . . . .	33
5.2. Constraints on stellar characteristics . . . . .	35
5.2.1. Stellar radius . . . . .	35
5.2.2. Stellar mass . . . . .	37
5.3. Constraints on exoplanet characteristics . . . . .	38
5.3.1. Planetary semi-major axis and inclination . . . . .	39
5.3.2. Planetary mass . . . . .	40
5.3.3. Planetary radius . . . . .	41
5.3.4. Planetary density . . . . .	42
5.3.5. Habitable zone . . . . .	42
5.3.6. Planetary surface temperature . . . . .	43
<b>6. Conclusions and summary</b>	<b>45</b>
<b>A. Tables for Kepler-21b</b>	<b>49</b>
<b>B. Tables and Figures for Kepler-10b</b>	<b>53</b>
<b>C. Tables and Figures for Kepler-22b</b>	<b>61</b>

# Nomenclature

## Parameters

Variable	(Physical) Parameter	Unit
$M$	Mass	kg
$R$	Radius	m
$\rho$	Density	kg/m <sup>3</sup>
$P$	Orbital period	s
$a$	Orbital semi-major axis	m
$i$	Orbital inclination	degree
$\Delta\nu$	Asteroseismic large frequency separation	$\mu\text{Hz}$
$\delta\nu$	Asteroseismic small frequency separation	$\mu\text{Hz}$
$T_{\text{eff}}$	Stellar effective Temperature	K
$m_v$	Apparent magnitude	mag
$\pi$	Stellar parallax	arcsecond
$BC$	Bolometric correction	mag
$K$	Radial velocity semi-amplitude	m/s
$g$	Surface gravity	m/s <sup>2</sup>

## Frequent indices

Index	Meaning
★	Star
⊙	Sun
⊕	Earth
P	(Exo-)Planet
AS	Asteroseismic

Index	Meaning
CL	'Classical'

## Constants

Constant	Meaning	Value
$G$	Gravitational constant	$6.674 \cdot 10^{-11} \text{ m}^3/\text{kg}\cdot\text{s}^2$
$M_{\odot}$	Mass of the Sun	$1.989 \cdot 10^{30} \text{ kg}$
$M_J$	Mass of Jupiter	$1.8986 \cdot 10^{27} \text{ kg}$
$M_{\oplus}$	Mass of the Earth	$5.9736 \cdot 10^{24} \text{ kg}$
$R_{\odot}$	Radius of the Sun	$696 \cdot 10^6 \text{ m}$
$R_J$	Radius of Jupiter	$71492 \cdot 10^3 \text{ m}$
$R_{\oplus}$	Radius of the Earth	$6378 \cdot 10^3 \text{ m}$
$\rho_{\odot}$	Mean density of the Earth	$1.408 \text{ g}/\text{cm}^3$
$\Delta\nu_{\odot}$	Large separation of the Sun (mean)	$135 \mu\text{Hz}$
$T_{\text{eff},\odot}$	Effective temperature of the Sun	$5778 \text{ K}$
$g_{\odot}$	Surface gravity of the Sun	$274 \text{ m}/\text{s}^2$
$M_{\text{bol},\odot}$	Absolute magnitude of the Sun	$4.74 \text{ mag}$
$L_{\odot}$	Luminosity of the Sun	$3.846 \cdot 10^{26} \text{ W}$

## Acronyms

Acronym	Meaning
AS	Asteroseismology/asteroseismic
HZ	Habitable zone
HR	Hertzsprung-Russell (diagram)
K-10	Kepler-10
K-21	Kepler-21
K-22	Kepler-22
KIC	Kepler Input Catalog
RV	Radial velocity



# 1. Introduction

Since the detection of the first exoplanet orbiting a main-sequence star, 51 Pegasi b, by Mayor & Queloz (1995) the astronomical efforts in detecting and characterizing further exoplanetary systems increased rapidly. Since today exoplanets got detected around a wide variety of stars (e.g., main sequence stars, M dwarfs,  $\delta$  Scu variables, giants) and in different classes of systems (e.g., binaries). Up to August 6, 2012, 777 exoplanets got detected (Schneider, 2012) using various types of techniques, e.g., doppler spectroscopy or transit photometry.

Besides the scientific interest in exoplanet systems to gain knowledge about, e.g., bulk composition, planetary system formation, planetary classes and population, it is one major goal to detect habitable planets. Alongside the scientific sensation, such a discovery would cause wide consequences, grazing mankind's perception of life itself.

Fullfilling these ambitious goals we need to improve our observation and analysis methods to reduce uncertainties in exoplanet parameters. Precise estimates of the fundamental stellar properties (stellar mass, radius and age) are required to constrain planetary characteristics. As we will see in the upcoming chapters, in most of the cases exoplanets get detected indirectly. The proof of their existence comes from observations of the stars. Thus, the derived planetary parameters depend directly on the known stellar properties.

If possible, properties of the stars are derived from a combined analysis of available data. The quality of the measured quantities depends on the accuracy of the observation and analysis methods. Usually stellar parameters are derived from observations with astrometric, spectroscopic or photometric techniques. Since the launch of spacecraft missions, capable of performing special uninterrupted runs, it is possible to combine these classical methods with asteroseismic analysis, i.e., studying the internal structure of pulsating stars by the interpretation of their frequency spectra. This can provide more precise knowledge about the host star, which translates into better knowledge about the exoplanet.

## *1. Introduction*

In this thesis I will compare the results obtained from classical studies with those including asteroseismic studies. I will emphasize the improvement in the precision of exoplanet parameters provided by asteroseismology. To get an idea what will be possible in the upcoming years, we also include two (possibly) launching space missions, i.e., Gaia and PLATO. Those will provide better data that allows to constrain exoplanet systems and their host stars even more precise. Due to the need of suitable data, I do the analysis for three Kepler planets: Kepler-10b, Kepler-21b and Kepler-22b. For all systems and different analysis methods I compare the derived uncertainties to weight the possible refinements.

## 2. Observing and modeling stars

In this chapter I introduce basic concepts about stellar observations and modeling. In Section 2.1 I describe the classical methods used in astrophysics and introduce the basic concepts of asteroseismology of Sun-like stars in Section 2.2.

### 2.1. Classical observations

#### 2.1.1. Astrometry

Astrometric techniques involve measurements of the position of stars and their movements in the celestial plane. The most important astrometric measurement is the stellar parallax

$$p['] = 1/d[\text{pc}], \quad (2.1)$$

where  $d$  is the distance of the star (see Figure 2.1).

Today the most important sources for parallaxes and proper motions of stars are the Hipparcos (Perryman & ESA, 1997, van Leeuwen, 2007) and Tycho-2 (Høg, 2000) catalogues, providing high-accuracy data. The Hipparcos data is limited in completeness from 7.3 mag and downwards. Usual uncertainties in the Hipparcos data are around 1 mas (Perryman & ESA, 1997).

#### 2.1.2. Photometry and Spectroscopy

By photometric measurements the flux of a stellar object can be obtained. The measured brightness of a star is called the apparent magnitude  $m$ . With knowledge of the distance  $d$  to the object or its parallax  $p$  this quantity translates to the absolute magnitude  $M$ :

$$m - M = 5 \log \left( \frac{d}{10 \text{ pc}} \right) = -5 \log(p) - 5. \quad (2.2)$$

## 2. Observing and modeling stars

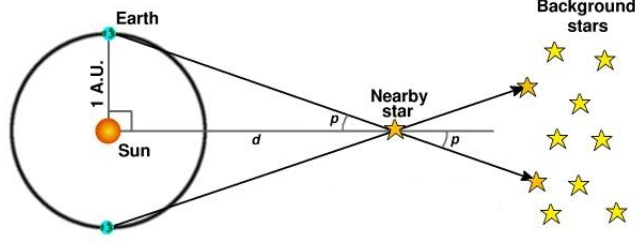


Figure 2.1.: STScI/NASA (2008) - Measuring trigonometric parallaxes.

Due to convention the absolute magnitude is equivalent to the apparent magnitude an object would have if it were 10 pc away from the observer and interstellar extinction were ignored. The total energy integrated over all wavelengths is called the bolometric magnitude  $M_{bol}$  (e.g., Gray, 2000). To transform absolute or apparent magnitudes in a specific bandpass (e.g., the  $V$  band around 540 nm) to bolometric magnitudes, a bolometric correction  $BC$  (e.g., Flower, 1996) is used. The zero point of the  $BC$  scale is set by reference to the Sun:

$$BC \equiv M_{bol,\odot} - M. \quad (2.3)$$

For Hipparcos data there exist associated bolometric corrections, given by Bessell (2007). The luminosity  $L_\star$  of a star can be derived directly from the known stellar magnitude (Valenti & Fischer, 2005):

$$\log \left( \frac{L_\star}{L_\odot} \right) = -0.4[M_V + BC - (M_{V,\odot} + BC_\odot)], \quad (2.4)$$

where  $M_V$  means the absolute magnitude in visual bandpass and the index  $\odot$  denotes solar values. To determine the radius and mass of a specific star I need as well its effective temperature  $T_{\text{eff}}$ , which is defined via the Stefan-Boltzmann law as the temperature of a blackbody radiator:

$$L_\star = 4\pi\sigma R_\star^2 T_{\text{eff}}^4, \quad (2.5)$$

with Boltzmann's constant  $\sigma$ . Valenti & Fischer (2005) use a spectrum-matching technique to estimate  $T_{\text{eff}}$ , as well as the surface gravity  $\log g_\star$ . Typical uncertainties for effective temperatures are around 40-70 K, but higher precision can be achieved (e.g., Kovtyukh et al., 2003). With these parameters I can now derive the radius

and mass of the star (e.g., Valenti & Fischer, 2005) using:

$$\frac{R_{\star}}{R_{\odot}} = \sqrt{\frac{L_{\star}}{L_{\odot}}} \left( \frac{T_{\odot}}{T_{\star}} \right)^2, \quad (2.6)$$

$$\frac{M_{\star}}{M_{\odot}} = \left( \frac{R_{\star}}{R_{\odot}} \right)^2 10^{\log(\frac{g_{\star}}{g_{\odot}})}. \quad (2.7)$$

## 2.2. Asteroseismology of solar-like stars

### 2.2.1. Introduction

Asteroseismology is the study of waves propagating through the stellar interior. Stars can be penetrated by sound and gravity waves. By observing and interpreting the resulting oscillations of the stars' lightcurves it is possible to carry information about the properties of stellar interiors and provide direct constraints on fundamental stellar parameters, e.g., stellar radii, masses, ages and initial chemical composition. Basic information of the theory of stellar oscillations can be found in, e.g., Cox (1980), Unno et al. (1989) or Aerts et al. (2010). Figure 2.2 illustrates which stars can be investigated with asteroseismology.

The description of stellar oscillations is separated into a spherical and a radial part. There are three "quantum numbers" to describe the oscillations. The *overtone*  $n$  is the number of radial nodes. The spherical part of the oscillations is described in terms of spherical harmonics with the angular degree  $l$  and the azimuthal order  $m$ , where  $l$  specifies the number of spherical nodes and  $|m|$  describes how many of the horizontal nodes are lines of longitude. Today's observations of distant stars with ground- and space-based instruments are surface-averaged, due to the huge distance. Therefore they are essentially sensitive only to modes of the lowest degree, for solar-like oscillations up to  $l = 2 - 3$  (Christensen-Dalsgaard, 2008).

### 2.2.2. Basic properties of stellar oscillations

In solar-like stars the observed modes are acoustic modes, i.e., acoustic waves trapped in spherical-shell cavities. They are known as p modes (pressure modes) and propagate with the speed of sound  $c = \sqrt{\gamma p / \rho}$  (with  $\gamma$  the first adiabatic exponent,  $p$  the pressure and  $\rho$  the density), which increases towards the centre of the star. For an assumed ideal gas law, it is  $p / \rho = T \mathcal{R} / \mu$ , with  $T$  the temperature,  $\mathcal{R}$  the gas constant and  $\mu$  the mean molecular weight. The modes are trapped between

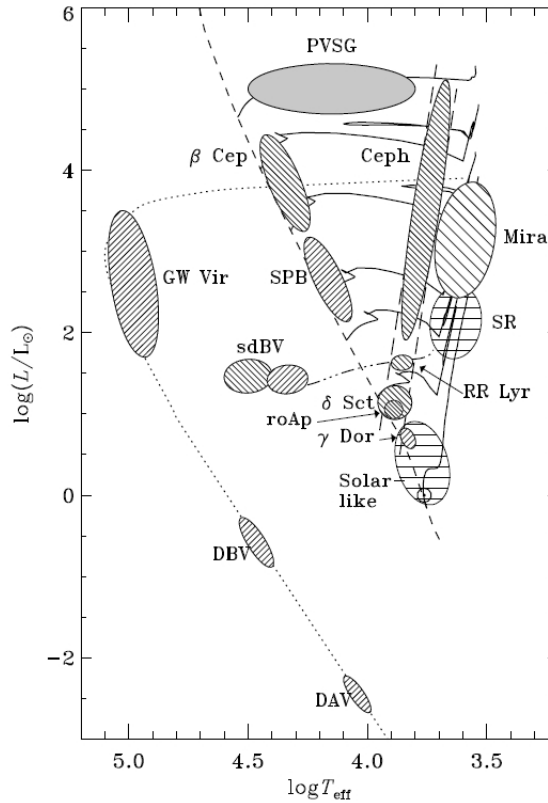


Figure 2.2.: Christensen-Dalsgaard & Thompson (2011) - Hertzsprung–Russell diagram for different classes of pulsating stars, which can be probed with asteroseismology. The hatching of the different zones classifies the excitation mechanism: slanted lines from lower right to upper left for heat-engine excitation of p modes, slanted lines from lower left to upper right for heat-engine excitation of g modes, and horizontal lines for stochastic excitation.

the near-surface region and an *inner turning point*  $r_t$ :

$$\frac{c(r_t)}{r_t} = \frac{\omega}{\sqrt{l(l+1)}}, \quad (2.8)$$

where  $r_t$  is the distance from the centre and  $\omega$  the angular frequency of the mode. Figure 2.3 shows an example for acoustic modes with their turning points.

Oscillations with turning points near the core carry information about the internal structure. For low-degree modes in the limit  $n \gg l$  Tassoul (1980) derived an

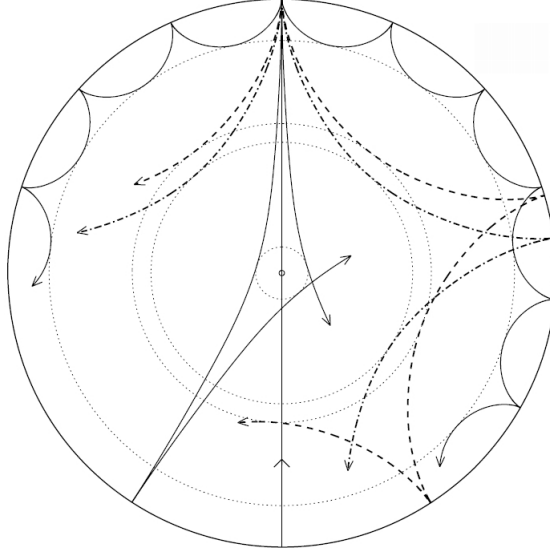


Figure 2.3.: Cunha et al. (2007) - Wave propagation for p modes in a cross-section of a solar-like star. We see acoustic ray paths, which are bend by the increase in sound speed with depth until the inner turning point is reached. There they undergo total internal refraction. At the surface the density decreases rapidly, thus the acoustic waves are reflected. The line passing through the centre illustrates the behaviour of a radial mode with  $l = 0$ .

asymptotic relation very important for the interpretation of solar-like oscillations:

$$\nu_{nl} \simeq \Delta\nu(n + l/2 + \epsilon) - [Al(l + 1) - B] \frac{\Delta\nu^2}{\nu_{nl}}, \quad (2.9)$$

where  $\nu_{nl} = \omega_{nl}/(2\pi)$  is the cyclic frequency of a mode with radial order  $n$  and degree  $l$  and

$$A = \frac{1}{4\pi^2\Delta\nu} \left( \frac{c(r_t)}{r_t} - \int_0^R \frac{1}{r} \frac{dc}{dr} dr \right). \quad (2.10)$$

$\epsilon = \epsilon(\nu)$  and  $B$  are determined by reflection properties near the surface (Gough, 1986).

According to the first term of Equation (2.9) modes with the same  $l$  and subsequent  $n$  are regularly spaced in frequency by the so called *large separation*  $\Delta\nu =$

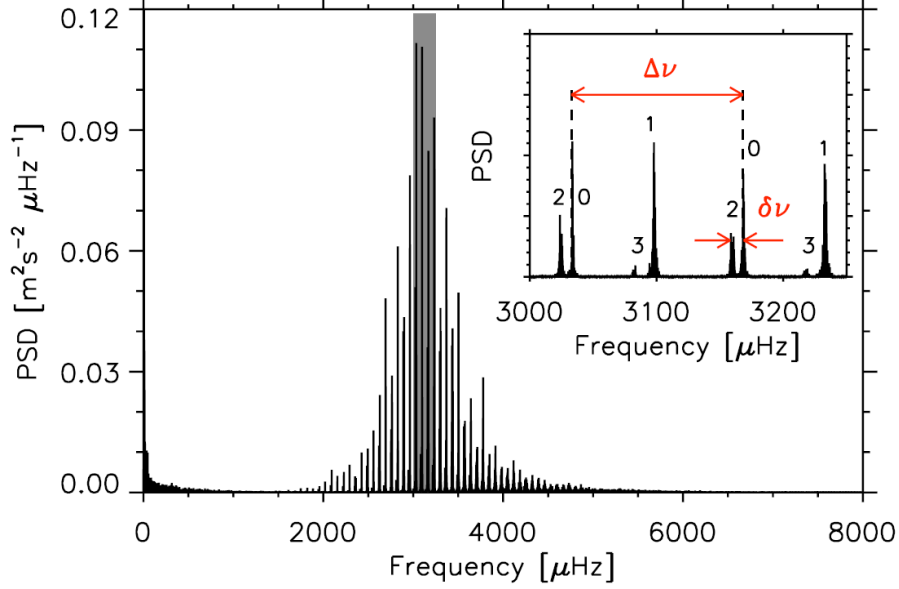


Figure 2.4.: Stahn (2011) - Solar power spectrum of a one year observation with the GOLF instrument on the SOHO spacecraft. The peaks in the grey-shaded section are shown in the inset, with the regular spacing (large und small separations) of the individual modes indicated with red arrows.

$\nu_{n-1l} - \nu_{nl}$ , which is the inverse sound travel time across a stellar diameter:

$$\Delta\nu = \left( 2 \int_0^R \frac{dr}{c} \right)^{-1}. \quad (2.11)$$

The large separation scales like the dynamical time scale and can be measured from the power spectrum. From Equation (2.11) follows for the mean density:

$$\Delta\nu \propto \rho^{1/2}. \quad (2.12)$$

The second terms of Equations (2.9) and (2.10) yield the *small frequency separation* (Gough, 1986)

$$\delta\nu_{nl} = \nu_{nl} - \nu_{n-1l+2} \simeq -(4l+6) \frac{\Delta\nu}{4\pi^2\nu_{nl}} \int_0^R \frac{1}{r} \frac{dc}{dr} dr, \quad (2.13)$$

which is sensitive to the properties of the sound speed variations in the core of the star.

In spherically symmetric stars the frequencies degenerate in  $m$ . Departures from



spherical symmetry like rotation lift this degeneracy and lead to approximated frequencies (in first order)

$$\omega_{nlm} \simeq \omega_{nl0} + m\langle\Omega\rangle, \quad (2.14)$$

with  $\langle\Omega\rangle$  an average of the angular velocity, weighted by the energy density of the mode (Christensen-Dalsgaard, 2008).

### 2.2.3. Other types of stellar oscillations

Due to the importance of other types of stellar oscillations, I will briefly note a second type of stellar oscillations.

For gravity (or g) modes the restoring force is buoyancy. A recent review of g modes can be seen in, e.g., Appourchaux et al. (2010). It is important to say that the detection of solar g modes is still a matter of debate.

### 2.2.4. Interpretation of stellar oscillation frequencies

As discussed in section 2.2.2 the large separation is directly linked to the mean density of a star, i.e.,  $\Delta\nu \propto \rho^{1/2}$ . Similar to this, Equation (2.13) shows a sensitivity to the sound speed gradient  $dc/dr$  near the stellar core. Due to the increase of the helium fraction and a decrease in the hydrogen content in the core over a star's lifetime, caused by nuclear burning, the mean molecular weight  $\mu$  increases over time. If one assumes the core temperature not to change much while the star remains on the main sequence, the sound speed decreases in the core and the ratio  $dc/dr$  gives a positive contribution to Equation (2.13). Hence, the small separation  $\delta\nu$  decreases as the star evolves and can be treated as an indicator for the star's age.

The asteroseismic Hertzsprung-Russell diagram in Figure 2.5 shows stellar evolutionary tracks for models with solar initial chemical composition and various stellar masses. It is obvious how measurements of the large and the small separation can be accurately related to mass and core hydrogen abundance. Hence, the evolutionary state can be determined. The accuracy of such mapping strongly depends on proper modeling, which is sensitive to stellar parameters, for instance, the heavy-element abundance, the initial hydrogen abundance or the mixing length parameter of convection (e.g., Christensen-Dalsgaard, 1993, Monteiro et al., 2002).

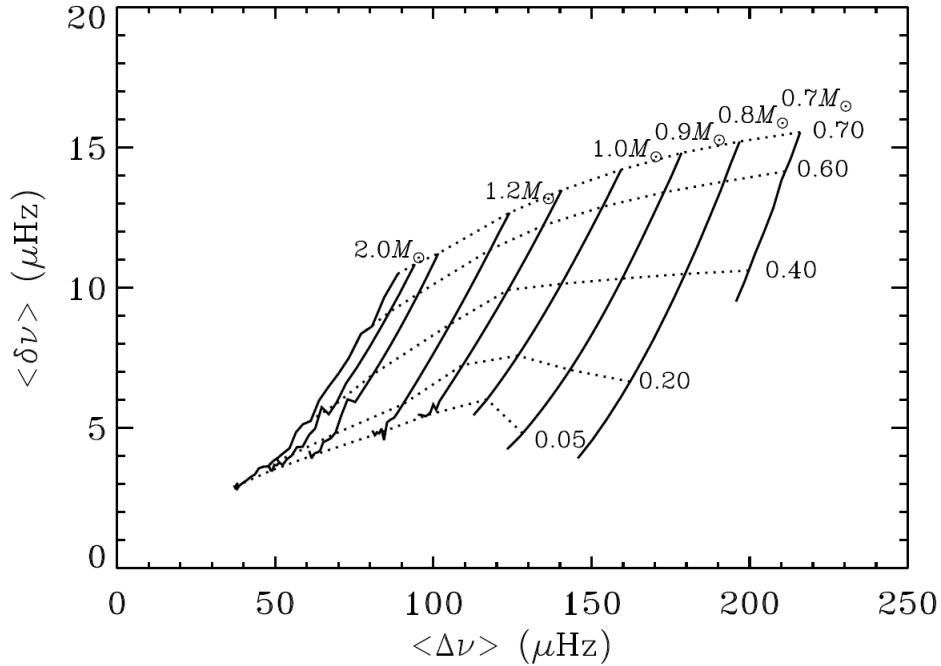


Figure 2.5.: Aerts et al. (2010) - Asteroseismic HR diagram. The large separation  $\Delta\nu$  is most sensitive to mass, the small separation  $\delta\nu$  is most sensitive to age. The solid, nearly vertical lines indicate stellar evolutionary tracks for stars with different initial mass, the nearly horizontal dashed lines are isopleths of constant hydrogen mass fraction in the core.

### 2.2.5. Classical vs. asteroseismic stellar modeling

Classical modeling, i.e., modeling not including seismic constraints, uses the star's location in the HR diagram and compare it with theoretical evolutionary tracks to determine mass, radius and age. The gain in knowledge by classical modeling is limited by several contributing factors, e.g., the uncertainties in stellar evolution theory, mostly due to poor knowledge of the internal mixing processes in stars, or the fact that the location in the HR diagram does not uniquely determine the properties of a star. Together with other uncertainties on physical processes like microscopic diffusion or rotational mixing the precision is strongly limited.

Models based on seismic analysis allow much tighter constraints, due to the precise measurements of the star's oscillation frequencies. Two basic approaches to such an analysis are known: *forward* and *inversion* techniques. Among the forward techniques, model fitting is often used to compare an observed data set with a set of frequencies predicted from a grid of stellar models. Then the best fit model is selected

and therefore yields seismic mass, radius and age of a star. Inversion techniques often use model independent methods and try to infer the internal density profile which is the best fit to the observation data set. By integrating over the stellar radius the mass can be computed.

Even if it is not possible to achieve individual frequencies for a star, it is at least possible to obtain average estimates of the large and small frequency separations. Those mean values can then be used together with  $L_*$ ,  $T_{\text{eff}}$ ,  $[Fe/H]$  and  $\log g_*$  for the modeling procedure. Thus, seismic modeling improves the precision on stellar parameters if it is possible to obtain at least rough estimates of the mean frequency separations. With measured individual frequencies, the seismic constraints may be even better.



# 3. Detecting and characterizing exoplanets

In this chapter I will start with an overview of today's detection methods for exoplanets in Section 3.1. I will focus on transit events and radial-velocity measurements, because those are used in my calculations. For completeness I give a brief introduction to other possibilities, i.e., astrometric, timing, microlensing and direct imaging methods.

Section 3.2 presents the model I use to probe the planetary systems studied in this thesis. I show the combination of RV and transit measurements to obtain the critical parameters of the exoplanetary systems. To deal with the short time period of a bachelor's thesis, several approximations and simplifications are made. The model depends strongly on the knowledge about the host star, implying  $M_\star$  and  $R_\star$  are already known.

## 3.1. Detection methods

### 3.1.1. Transit events

When a planet passes in front of its host star in the line of sight of an observer, some of the light gets blocked. Thus, the observer can monitor a tiny dip in the lightcurve. The amount of the dimming depends on the ratio of the areas of the projected disks of planet and star. This results in the transit depth

$$\frac{\Delta F}{F} \equiv \frac{F_{\text{no transit}} - F_{\text{transit}}}{F_{\text{no transit}}} = \left( \frac{R_p}{R_\star} \right)^2, \quad (3.1)$$

where  $F$  refers to the measured flux and  $R_p$  to the exoplanet radius. A precise estimate of the planetary radius requires a precise estimate of the radius of the host star. Figure 3.1 shows an example from the CoRoT mission. In Section 3.2.1 I will

### 3. Detecting and characterizing exoplanets

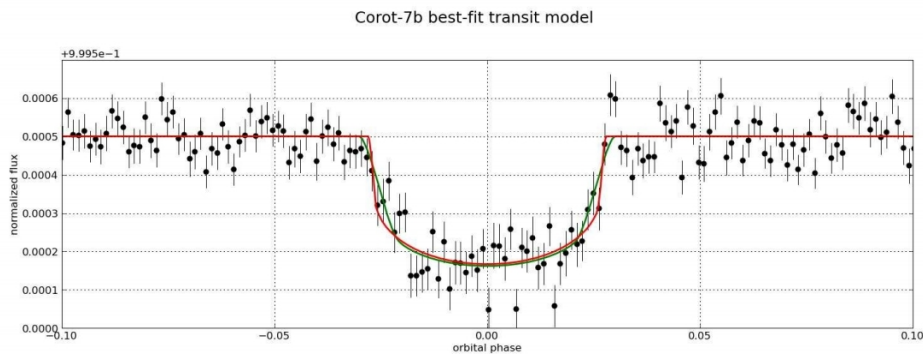


Figure 3.1.: Léger et al. (2009) - Transit light curve of CoRoT-7b. The dots indicate the measured flux with corresponding errorbars, the solid lines are two fits, using different types of light curve models.

present a more analytic approach to the transit light curves.

There are several disadvantages in transit observations (Haswell, 2010). First of all, the likelihood  $p$  that a randomly orientated exoplanet lies in the line of sight of an observer decreases dramatically with increasing semi-major axis  $a_p$  of the planetary orbit:

$$p_{\text{transit}} = \frac{R_{\star} + R_p}{a_p(1 - e^2)} \approx \frac{R_{\star}}{a_p}, \quad (3.2)$$

which is simplified for  $R_{\star} \gg R_p$  and circular orbits (eccentricity  $e = 0$ ). The expected number of planet discoveries for transit search programmes scales like (Haswell, 2010):

$$\text{transit detection probability} \propto R_p^2 a_p^{-7/4} L_{\star}^{3/2} R_{\star}^{-5/4}. \quad (3.3)$$

These quantified selection effects are in favour of large and close-in planets with luminous and small host stars.

A further disadvantage is a high rate of false detections, which could be caused by several reasons. The most common sources seem to be:

- blended eclipsing binary systems,
- grazing eclipsing binary systems with equal-mass components,
- transits by planet-sized stars.

Therefore, planet candidates always need independent confirmation to rule out

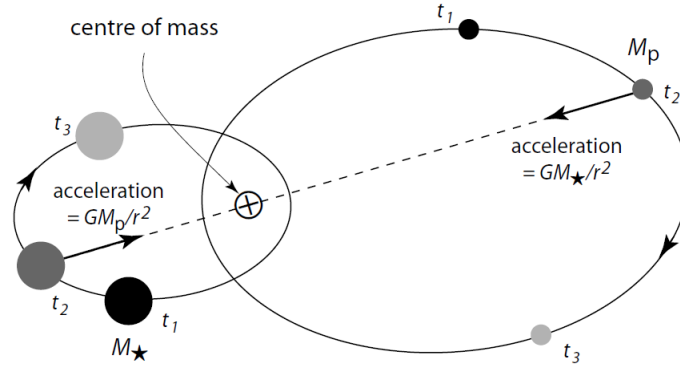


Figure 3.2.: Perryman (2011) - Exoplanet and its parent star orbiting around their common barycentre. The Doppler shift of the emitted light from the star can be used to determine its minimum mass.

false detections. Typically this is done by radial velocity measurements to obtain the object's mass.

### 3.1.2. Doppler spectroscopy

Radial velocity measurements use spectroscopic methods to obtain the projected motion of a star as it orbits the system's barycentre, illustrated in Figure 3.2. This can be done by measuring the Doppler shift of the emitted light which is sensitive only to the motion along the line of sight.

For my purposes the most important aspect on radial velocities is the RV semi-amplitude (Perryman, 2011):

$$K \equiv \frac{2\pi}{P_\star} \frac{a_\star \sin i_\star}{\sqrt{1 - e_\star^2}}, \quad (3.4)$$

with period  $P_\star$ , semi-major axis  $a_\star$ , eccentricity  $e_\star$  and inclination  $i_\star$  of the stellar orbit. A radial-velocity curve can be seen later in Figure 4.1. By combining the above equation with Kepler's third law of planetary motion I get an estimate of the minimum mass of the planet (see Section 3.2.2).

### 3.1.3. Other methods

#### Astrometry

High-accuracy astrometric measurements (like described in Section 2.1.1) can be used similar to Doppler spectroscopy to calculate the star's motion in the plane of the sky around the barycentre. For circular orbits the astrometric signature (Perryman, 2011)

$$\alpha = \frac{M_p}{M_\star + M_p} a \simeq \frac{M_p}{M_\star} a \equiv \left( \frac{M_p}{M_\star} \right) \left( \frac{a}{1 \text{ AU}} \right) \left( \frac{d}{1 \text{ pc}} \right)^{-1} \text{ arcsec} \quad (3.5)$$

is particularly sensitive to long orbits. In this technique the motion around the barycentre must be discerned from the stars proper motion and the reflex motion (its parallax), due to the Earth's motion around the Sun. Until today nearly 500 planets got detected using radial velocity or astrometric methods (Schneider, 2012).

#### Timing

The changes in radial velocity and astrometric position lead to periodic oscillations of the position of the host star around the system's barycentre. Due to the light travel time there can be anomalies in the measured period, from which we can conclude on an exoplanet. The amplitude

$$\tau_p = \frac{1}{c} \frac{a M_p \sin i}{M_\star} \quad (3.6)$$

is related to the displacement of the star and gives an estimate for the planetary mass.  $c$  is the speed of light. Until today around 15 planets go detected this way (Schneider, 2012).

#### Microlensing

Due to the distortion of spacetime in general relativity, the light from distant background stars could be bent by the gravitational potential of a foreground object. Under certain conditions this could happen to exoplanets, from which several constraints on the planetary system can be derived (Perryman, 2011). Until today around 16 planets got detected this way (Schneider, 2012).



## Imaging

Imaging refers to techniques trying to receive a point source image of the exoplanet. The planet to star flux ratio is extremely small, hence it is quite hard to receive resolutions and precisions high enough for such images. Nevertheless it is possibly the only way in the future to obtain resolved spatial images of exoplanets surfaces and better spectroscopic investigations. Until today around 30 planets got detected this way (Schneider, 2012).

## 3.2. Describing exoplanetary orbits

### 3.2.1. Inferences from transit light curves

The light curve of a transit event can yield various physical quantities on the planetary system, depending on the precision of the observation and the made assumptions. To shorten the procedure, to highlight the main goal of comparing astero-seismic and classical analysis, and due to the non-availability of public Kepler data of the program stars, I pass over the process of deriving parameters from the light curves itself. Instead of applying standard modeling of the light curves, I take the required parameters of the exoplanet systems from the main publications and insert them in the equations. Tables 4.1, 4.2 and 4.3 reveal the corresponding parameters.

For the following description of the planet and star parameters I use two standard assumptions:

- The mass of the exoplanet is negligible compared to its host-star ( $M_p \ll M_\star$ ).
- The planetary orbit is approximated to be circular (eccentricity  $e = 0$ ).

Figure 3.3 shows the profile of a transit light curve with the basic observables: orbital period  $P$ , transit depth  $\Delta F$  and total transit duration  $t_T$ . The fully occulted transit duration  $t_F$  depends strongly on the characteristics of the light curve. In nearly all exoplanet systems this part is not a flat-bottomed dip. In Equation (3.1) I implicitly assumed that the stellar disc has a uniform brightness, which is not strictly valid, as we can see in Figure 3.1. For a correct treatment of this effect, called stellar limb darkening, see, e.g., Haswell (2010). I neglect the limb darkening in my study and apply Equation (3.1) without further assumptions.

### 3. Detecting and characterizing exoplanets

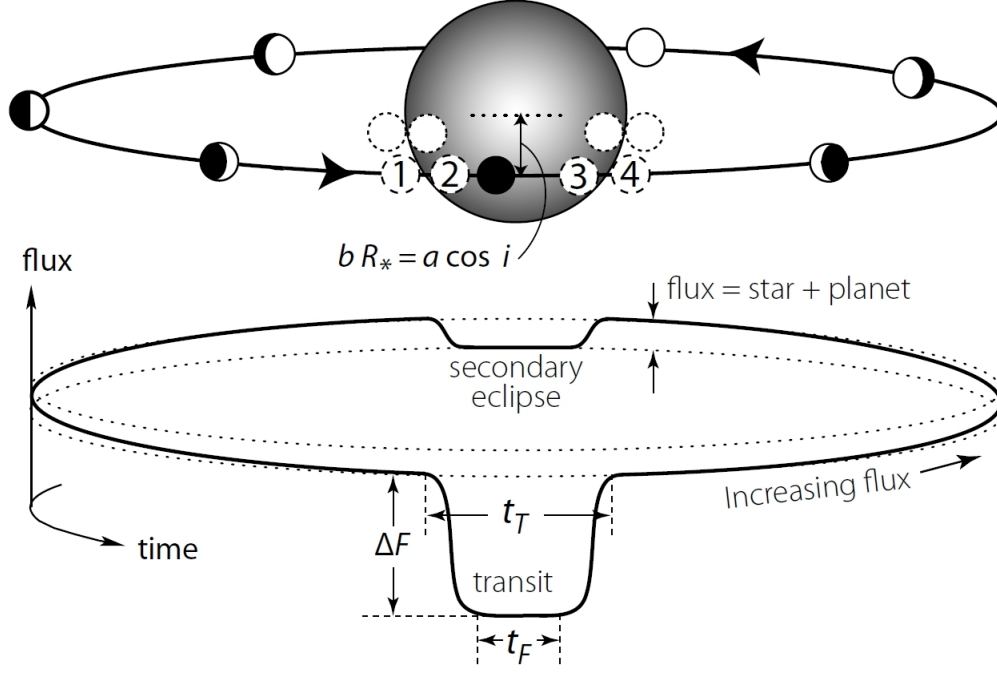


Figure 3.3.: Perryman (2011) - Schematic of a transit, showing the four basic observables from a transit light curve: The orbital period  $P$  is the time needed for a full circuit by the exoplanet. The transit depth  $\Delta F$  gives the difference in flux with and without transit. The total transit duration  $t_T$  reaches from the first to the fourth contact of the planetary disk in front of the host star and finally the fully occulted transit duration  $t_F$  means the time between second and third contact. The secondary eclipse can sometimes be observed when the planet vanishes behind its star.

Now for setting up an analytic description<sup>1</sup> of the planetary parameters, I start using Kepler's third law of planetary motion

$$\frac{P^2}{a^3} = \frac{4\pi^2}{G(M_\star + M_p)} \simeq \frac{4\pi^2}{GM_\star} \quad (3.7)$$

to relate the period  $P$  of the exoplanet to the semi-major axis  $a$  of its orbit, where  $G$  denotes the gravitational constant.

The impact parameter (see Figure 3.3)

$$b \equiv \frac{a}{R_\star} \cos i \quad (3.8)$$

<sup>1</sup>From now on all non-labeled parameters are *planetary* parameters.

is geometrically defined as the projected distance between the planet and star centres during mid-transit in units of  $R_\star$  and can be deduced from the modeling of the transit light curve. With Equations (3.7) and (3.8) I calculate the orbital inclination. Finally, Equation (3.1) trivially converts to the planetary radius.

### 3.2.2. Combining transit and radial velocity measurements

To obtain an estimate of the planetary mass, I need to combine the measurements from radial velocity with the outcome from the transit analysis. According to Cumming et al. (1999) the radial velocity semi-amplitude from Equation (3.4) can be combined with Kepler's third law to get the following estimate:

$$K_\star = \left( \frac{2\pi G}{P} \right)^{1/3} \frac{M_p \sin i}{(M_\star + M_p)^{2/3} \sqrt{1 - e^2}}, \quad (3.9)$$

which is used to calculate the minimum planetary mass:

$$M_p \sin i \simeq \left( \frac{P}{2\pi G} \right)^{1/3} K_\star M_\star^{2/3}. \quad (3.10)$$

If a transit can be observed,  $\sin i \approx 1$  and its exact value is known from Equation (3.8). With this knowledge I convert the lower limit from Equation (3.10) into an absolute value for the planetary mass.

### 3.2.3. Habitability of exoplanets

To give some considerations on the important question of the suitability of a planet for the evolution of life I also check the effects on essential parameters. Three crucial parameters determining the habitability of an exoplanet are its density, the distance from its host star and its surface temperature.

The density is computed using  $\rho = M/R^3$  in Earth units and affects interior properties, e.g., the bulk composition.

The distance to the star is crucial for the question whether it lies in the habitable zone of the host star. I define the habitable zone as the zone around the star where a planet with the bond albedo of the earth ( $\alpha = 0.29$ , Borucki et al., 2012) can habit liquid water. With this definition the inner boundary of the HZ is the distance to the star at which the radiative equilibrium temperature  $T_{\text{eq}}$  of the planet drops below  $373\text{ K}$ . The outer boundary is the distance at which it drops below  $273\text{ K}$ .

### 3. Detecting and characterizing exoplanets

Following Borucki et al. (2012), this radius is given by:

$$R_{\text{HZ}} = \sqrt{\frac{1 - \alpha}{4\beta}} R_{\star} \left( \frac{T_{\text{eff}}}{T_{\text{eq}}} \right)^2. \quad (3.11)$$

$\beta$  is defined as the fraction of the surface of the planet that reradiates the absorbed flux and is set to  $\beta = 1.0$  for a rapidly rotating body with a strongly advecting atmosphere (Borucki et al., 2012).

Finally, the surface temperature of the planet is important for liveable conditions on the planet’s surface. It is also computed with Equation (3.11), using the appropriate semi-major axis of the planetary orbit for the distance to the host star.

## 3.3. Exoplanet detection programmes

In the following sections I describe observational programmes which are used or needed for the calculations. For each type I give a current state-of-the-art example.

### 3.3.1. Radial velocity instruments

Current survey instruments which are used for radial velocity exoplanet searches are mostly échelle spectrographs. Those spectrographs use special types of diffraction gratings with relatively low groove densities, optimized for high diffraction orders (e.g., Nagaoka & Mishima, 1923). As an example for today’s state-of-the-art échelle spectrographs I will give a short description of Keck/HIRES, which is highly used for follow-up observations of Kepler candidates.

#### Keck/HIRES

HIRES is the échelle spectrograph at the Keck I 10-m telescope on Mauna Kea, Hawaii. Its accuracy in the configuration of Vogt et al. (2000) reaches the resolving power of  $R = \lambda/\Delta\lambda = 80000$ . The according spectra span from 390 to 620 nm in wavelength range. Its precision for radial velocity measurements is up to 1 m/s, which is required to detect Earth-type planets in the habitable zone around Sun-like stars.

### 3.3.2. Transit searches from space

For ground-based photometry it is complicated to reach accuracies better than 0.1 % (which is necessary for the detection of small planets) because of several limiting factors like, e.g., atmospheric extinction. Space-based observations lack most of these problems and additionally offer the possibility of long uninterrupted runs, independent of day-night-cycles. The current two most important spacecrafts dedicated to exoplanet science (and asteroseismology) are the CNES-led mission CoRoT and the NASA-led mission Kepler. Because I use three Kepler planets in this thesis, I will only describe the most important characteristics of Kepler.

#### Kepler

The NASA Kepler satellite (Borucki et al., 2010) was launched on March 6th, 2009 into an heliocentric orbit, comprising a 0.96 m telescope. Like CoRoT it is dedicated as well to exoplanet science and asteroseismology. It has 42  $2k \times 1k$  CCDs which cover an observational field of about 115 square degrees. The wavelength ranges from 430 to 890 nm and it monitors around 150000 main sequence stars in the magnitude range from 8 to 15. Most of the observed stars range from  $V \sim 10.5 - 15$ , very few are brighter. Until today NASA (2012) lists over 70 confirmed exoplanets and around 2300 planet candidates, detected by the Kepler spacecraft.

### 3.3.3. Future observations

In the numerical analysis I give a prospect of possibilities in the upcoming years. For this reason I introduce two planned missions, dedicated to exoplanet science.

#### PLATO

PLATO is a mission under consideration by ESA (Catala, 2009). Like CoRoT and Kepler it will be dedicated to exoplanet observations and asteroseismology. Its observational field will be significantly wider than those of CoRoT and Kepler and will focus on brighter stars (around 100000 stars with  $V \sim 4 - 11$  and around 400000 with  $V \leq 13$ ) with short-cadence uninterrupted monitoring. The current plans for PLATO contain a payload constructed of about 28 identical small, very wide-field telescopes with the same  $26^\circ$  diameter field. The main advantages of PLATO compared to current missions will be its ability to observe significantly

### *3. Detecting and characterizing exoplanets*

smaller Earth-size exoplanets in the habitable zone of Sun-like stars, as well as planets orbiting hotter (brighter) stars. Following Catala (2011) the asteroseismic analysis of the PLATO light curves will be able to provide 1-4 % errors in the stellar masses, which will lead to an improvement of planetary mass estimates.

#### **Gaia**

The Gaia mission of ESA (Lindegren, 2009) is due for launch in 2013 into the Lissajous-type orbit around L2. It contains 3 different instruments dedicated to astrometric, photometric and spectroscopic observations. The telescope consists of two  $1.4 \times 0.5 \text{ m}^2$  mirrors. It will survey approximately a billion stars from  $V \sim 6-20$  mag and will provide extremely detailed measurements of distances, parallaxes and annual proper motions with a precision of about  $20 \mu\text{as}$ . Spectrophotometric measurements of luminosity, effective temperature, gravity and chemical composition of the stars will be made, which will give (among other things) estimates of their radii up to a precision of around 2% (Bailer-Jones, 2002).

## 4. Numerical experiment

In this study I am mainly interested in a comparison of the expected precision of various seismic and non-seismic methods rather than absolute values.

To deal with the numerical calculations, I used the IDL platform (Exelis Visual Information Solutions, 2012) in version 6.3, licensed by the 'Institut für Astrophysik, Universität Göttingen'.

In this section I describe the different methods to determine the uncertainties in exoplanet properties and to understand which factors contribute the most to possible changes. I firstly present the three studied exoplanet systems in Section 4.1. After that I explain the different analysis methods in Section 4.2.

### 4.1. Analyzed exoplanet systems

All three exoplanets I studied are Kepler planets. The reason for this is that I need exoplanet systems, which got probed with asteroseismic methods. This limits the number of possible systems dramatically. Furthermore I look for systems with small planets, preferably around the size of the Earth. The Kepler planets 10b, 21b and 22b suit well to these criteria.

#### 4.1.1. Kepler-21

Kepler-21b (Howell et al., 2012) is the main target of this study and mainly interesting due to its supposed high density and therefore rocky composition. Its host star is the only of the three exoplanet systems, for which a precise parallax is known from Hipparcos. Accordingly, it is possible to compare classical methods with asteroseismology in a satisfactory way. Unfortunately, the precision of the RV measurements is quite bad (see Figure 4.1), which prevents from calculating a good estimate for the planetary mass. The upper limit of the RV amplitude is  $K < 3.9 \pm 5.4 \frac{m}{s}$ , hence the values of planetary mass and density derived in my work are also upper limits. Basic properties of Kepler-21b and its host star are given in Table 4.1.

#### 4. Numerical experiment

	Parameter [Unit]	Value $\pm$ Error	Procedure	Reference
Star	$m_v$ [mag]	$8.3723 \pm 0.0018$	A/B/C	van Leeuwen (2007)
	$\pi$ ["]	$0.00886 \pm 0.00058$	A/B/C	van Leeuwen (2007)
	BC [mag]	-0.021	A/B/C	Bessell (2012)
	$T_{\text{eff}}$ [K]	$6250 \pm 250$	A/B/C	Howell et al. (2012)
	$\log g_{\star}$ [ $\log \frac{m}{s^2}$ ]	$4.00 \pm 0.25$	A/B/C	Howell et al. (2012)
	$K$ [ $\frac{m}{s}$ ]	$3.9 \pm 5.4$	A/B/C/D/E	Howell et al. (2012)
	$\Delta\nu$ [ $\mu\text{Hz}$ ]	$60.86 \pm 0.55$	B/C	Howell et al. (2012)
	$R_{\star,\text{cl}}$ [ $R_{\odot}$ ]	$1.83 \pm 0.19$	A/B/C	Equation (2.6)
	$M_{\star,\text{cl}}$ [ $M_{\odot}$ ]	$1.22 \pm 0.75$	A/B/C	Equation (2.7)
	$R_{\star,\text{as}}$ [ $R_{\odot}$ ]	$1.86 \pm 0.02$	D/E	Howell et al. (2012)
	$M_{\star,\text{as}}$ [ $M_{\odot}$ ]	$1.34 \pm 0.01$	D/E	Howell et al. (2012)
Planet	$P$ [days]	$2.785755 \pm 0.000034$	A/B/C/D/E	Howell et al. (2012)
	$R_p/R_{\star}$ [ $R_{\star}$ ]	$0.00806 \pm 0.00019$	A/B/C/D/E	Howell et al. (2012)
	$b$ [ $R_{\star}$ ]	$0.640 \pm 0.028$	A/B/C/D/E	Howell et al. (2012)

Table 4.1.: Stellar and planetary properties for the Kepler-21 system. The entries in the third column show for which calculation method the different values are used. See Section 4.2 for details.

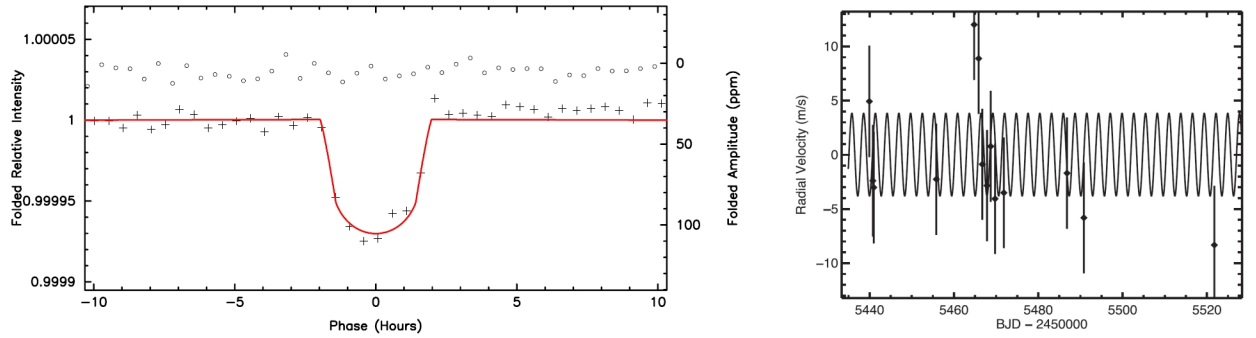


Figure 4.1.: Kepler-21 (Howell et al., 2012) - Left panel: Detrended, binned and phase-folded transit data. The crosses represent individual observations, circles represent residuals, the red line shows the overplotted model-fit, which included stellar limb-darkening. Right panel: RV measurements (diamonds) for HD 179070 (Kepler-21) from Keck/HIRES. The error bars are composed of internal errors of  $\sim 2 \text{ m s}^{-1}$ , which are added in quadrature to  $5 \text{ m s}^{-1}$  to account for the large uncertainties. The solid line is a fit of a Keplerian orbit to the measured velocities.

#### 4.1.2. Kepler-10 and Kepler-22

Kepler-10 (Batalha et al., 2011) and Kepler-22 (Borucki et al., 2012) also suit to the criteria and are interesting due to the small planetary radius of Kepler-10b and the position of Kepler-22b in the habitable zone.



	Parameter [Unit]	Value $\pm$ Error	Procedure	Reference
Star	$\log g_\star$ [ $\log \frac{m}{s^2}$ ]	$4.54 \pm 0.10$	A/B/C	Batalha et al. (2011)
	$K$ [ $\frac{m}{s}$ ]	$3.3 \pm 1.0$	A/B/C/D/E	Batalha et al. (2011)
	$\Delta\nu$ [ $\mu\text{Hz}$ ]	$118.2 \pm 0.2$	B/C	Batalha et al. (2011)
	$R_{\star,\text{cl}}$ [ $R_\odot$ ]	$0.98 \pm 0.49$	A/B/C	Kepler Mission Team (2009)
	$M_{\star,\text{cl}}$ [ $M_\odot$ ]	$1.22 \pm 1.25$	A/B/C	Equation (2.7)
	$R_{\star,\text{as}}$ [ $R_\odot$ ]	$1.056 \pm 0.021$	D/E	Batalha et al. (2011)
	$M_{\star,\text{as}}$ [ $M_\odot$ ]	$0.895 \pm 0.06$	D/E	Batalha et al. (2011)
Planet	$P$ [days]	$0.837495 \pm 0.000005$	A/B/C/D/E	Batalha et al. (2011)
	$R_p/R_\star$ [ $R_\star$ ]	$0.01232 \pm 0.00016$	A/B/C/D/E	Batalha et al. (2011)
	$b$ [ $R_\star$ ]	$0.339 \pm 0.079$	A/B/C/D/E	Batalha et al. (2011)

Table 4.2.: Stellar and planetary properties for the Kepler-10 system. The entries in the third column show for which calculation method the different values are used. See Section 4.2 for details.

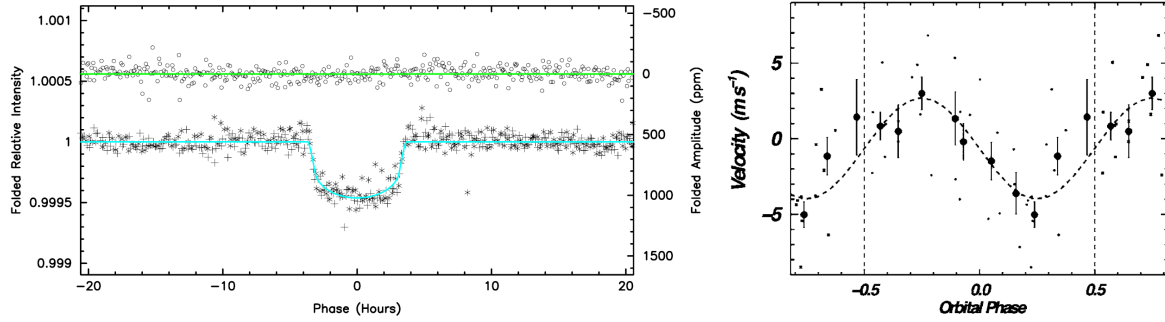


Figure 4.2.: Kepler-10 (Batalha et al., 2011) - Left panel: Phase-folded light curve centered on phase zero for Kepler-21b. The blue line shows the modeled light curve, the green line corresponds to a model of the phase cutout of the light curve. Right panel: RV signal vs. phase for Kepler-10. The small points are the individual observations. The larger points with error bars are derived from the spread in individual points as average over 0.1 phase bins. At this magnitude level this RV measurement is the limit for ground based observations and can't be improved with current capabilities.

Their corresponding stellar and planetary properties are given in Table 4.2 and 4.3 respectively.

For both stars I couldn't find estimates on the stellar parallax, as well as on the stellar magnitude in visual band, which prevents computing the stellar radius and mass without seismic values. For the non-seismic estimates of the stellar radius I use data from the Kepler Input Catalog (Kepler Mission Team, 2009) and make a guess for the corresponding precision (see following subsection).

#### 4. Numerical experiment

	Parameter [Unit]	Value $\pm$ Error	Procedure	Reference
Star	$\log g_\star$ [ $\log \frac{m}{s^2}$ ]	$4.44 \pm 0.06$	A/B/C	Borucki et al. (2012)
	$K$ [ $\frac{m}{s}$ ]	$4.9 \pm 7.4$	A/B/C/D/E	Borucki et al. (2012)
	$\Delta\nu$ [ $\mu\text{Hz}$ ]	$137.5 \pm 1.4$	B/C	Borucki et al. (2012)
	$R_{\star,\text{cl}}$ [ $R_\odot$ ]	$1.14 \pm 0.57$	A/B/C	Kepler Mission Team (2009)
	$M_{\star,\text{cl}}$ [ $M_\odot$ ]	$1.31 \pm 1.32$	A/B/C	Equation (2.7)
	$R_{\star,\text{as}}$ [ $R_\odot$ ]	$0.979 \pm 0.02$	D/E	Borucki et al. (2012)
	$M_{\star,\text{as}}$ [ $M_\odot$ ]	$0.97 \pm 0.06$	D/E	Borucki et al. (2012)
Planet	$P$ [days]	$289.8623 \pm 0.0020$	A/B/C/D/E	Borucki et al. (2012)
	$R_p/R_\star$ [ $R_\star$ ]	$0.0222 \pm 0.0012$	A/B/C/D/E	Borucki et al. (2012)
	$b$ [ $R_\star$ ]	$0.768 \pm 0.132$	A/B/C/D/E	Borucki et al. (2012)

Table 4.3.: Stellar and planetary properties for the Kepler-22 system. The entries in the third column show for which calculation method the different values are used. See Section 4.2 for details.

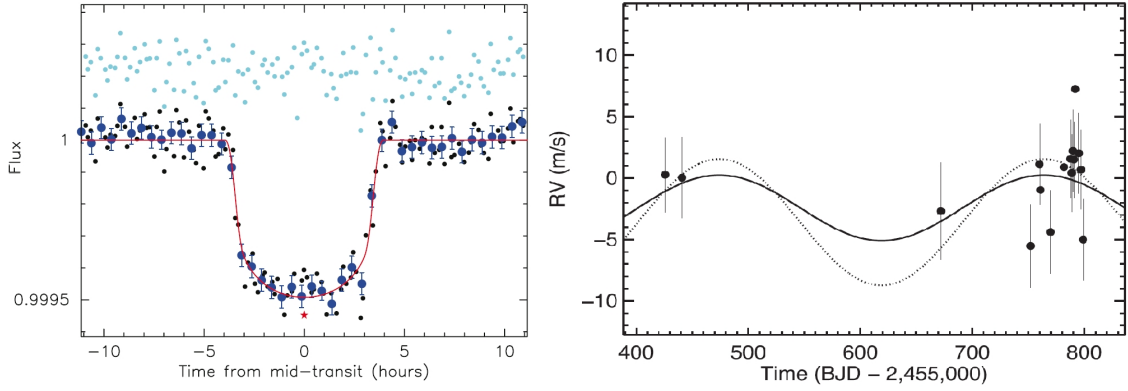


Figure 4.3.: Kepler-22 (Borucki et al., 2012) - Left panel: Folded light curve with model fit in red. The black dots represent individual observations, dark blue points represent 30 minute binned data, cyan points represent residuals after fitting. Right panel: RV measurements with a circular orbit fit for a planetary mass of  $19 M_\oplus$  (solid line) and  $27 M_\oplus$  (dashed line).

For Kepler-10 the RV measurements (see Figure 4.2) are precise enough to allow realistic mass and mean density estimates with implications on the planetary interior and bulk composition. For Kepler-22 this is not possible in a satisfactory way, due to the low precision of the RV measurements (Figure 4.3).

As for Kepler-21b the shown values of the RV measurements are upper limits, which translates into upper limits for planetary mass and density.

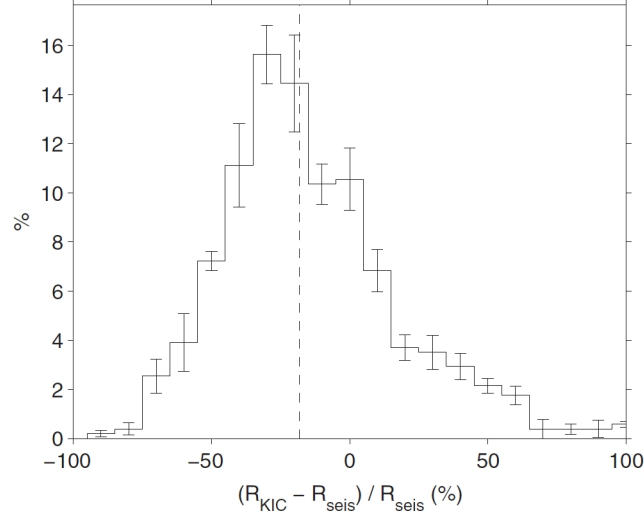


Figure 4.4.: Verner et al. (2011) - Distribution of the difference between KIC and seismic radii. Error bars show the standard deviation in each range when determined using all possible combinations of model grid and input data. The dashed line shows the median of the distribution.

### Precision of stellar radii from the KIC for K-10 and K-22

Verner et al. (2011) examine the precision of the KIC parameters, including the radius. Figure 4.4 (adopted by Verner et al., 2011) provides a first estimate on the precision and reveals that the data suffers from strong systematic errors. The paper compares the KIC radius to asteroseismic radii, computed with measured frequency separations. The median of the distribution is a little less than  $\frac{\Delta R_{\star}}{R_{\star}} \simeq 0.25$ .

Because there is no guarantee on the correctness of this estimate and to include some statistical informations I imply a second evaluation on the uncertainties. Valenti & Fischer (2005) computed error estimates for a representative sample of 1040 F, G and K dwarfs on the main-sequence. My calculation of the classical values for the stellar mass and radius via Equations (2.6) and (2.7) is build on their paper. Figure 4.5 shows the relative uncertainty of the spectroscopic radius estimate as a function of magnitude, where the uncertainty increases dramatically towards darker stars. For stars with  $V > 11$  I expect a relative uncertainty of the radius estimate of  $\frac{\Delta R_{\star}}{R_{\star}} \simeq 0.25$ .

From a linear summation of the systematic error from Verner et al. (2011) and the statistical error from Valenti & Fischer (2005) I assume an error of  $\frac{\Delta R_{\star}}{R_{\star}} \simeq 0.5$  for the radius values of the KIC for Kepler-10 and Kepler-22.

#### 4. Numerical experiment

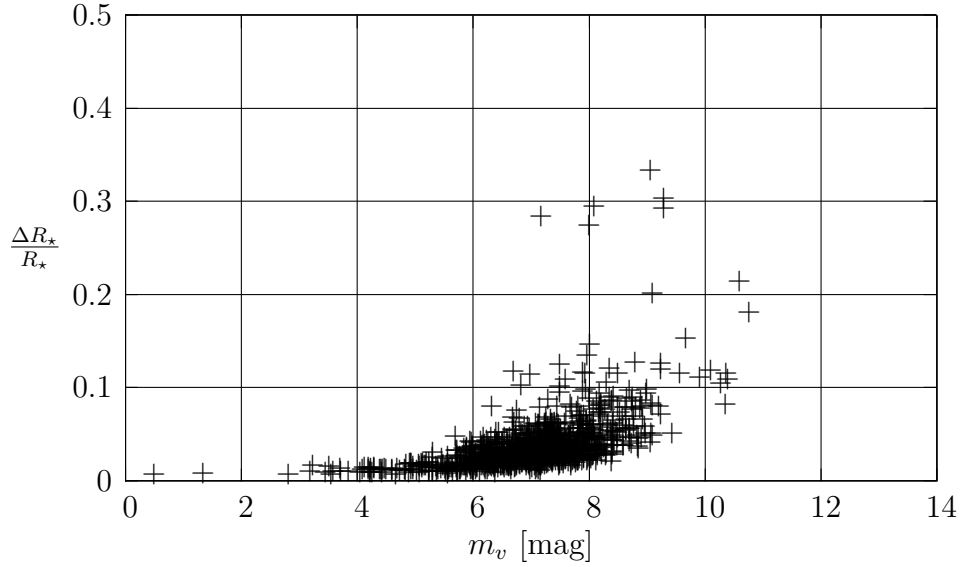


Figure 4.5.: Visual magnitude of 1040 F, G and K stars versus their relative errors in radius. With data from Valenti & Fischer (2005).

## 4.2. Methods of the parameter study

### 4.2.1. Stellar parameters

I start by calculating the crucial parameters of the host star. This phase is essential since uncertainties in the stellar properties determine the precision of the inference of the exoplanet parameters. I compute the stellar mass and radius using different seismic and non-seismic methods and compare their respective precisions.

In order to compare the influence of the precision of the stellar parameters on the exoplanet properties and to eliminate inflections from changing parameters I set the absolute values of the stellar parameters to the corresponding seismic value at the end of the stellar calculations. Thus, the absolute values of the stellar mass and radius (not the corresponding errors!) will be the same for the calculation of the planetary characteristics for each method. The correctness of this setting will be discussed and validated in Section 5.1.

#### Procedure A - Classical approach

The 'classical' approach serves as basis for procedure B and C. As a starting point I calculate the stellar luminosity with Equation (2.4). Combined with Equation (2.6) and (2.7) for the radius and the mass, yields the main stellar parameters.

For Kepler-10 and Kepler-22 there don't exist precise estimates for the parallax. Instead, I take the radius for those stars from the Kepler Input Catalog (Kepler Mission Team, 2009) and compute the mass using Equation (2.7). See Section 4.1.2 for an estimate of the precision of this adoption.

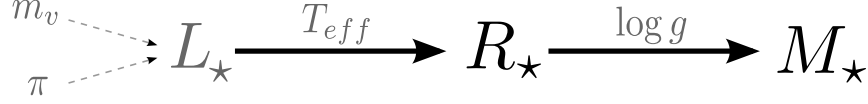


Figure 4.6.: Procedure A - Processing diagram to derive the 'classical' radius and mass of the host star.

### Procedure B - Asteroseismic mass constraint

From now on I use seismic observables to constrain the stellar properties. In this first approach the radius of the star is fixed to the classical value from above. The mass of the star is computed using Equation (2.12):

$$\frac{M_{\star}}{M_{\odot}} = \left( \frac{\Delta\nu_{\star}}{\Delta\nu_{\odot}} \right)^2 \left( \frac{R_{\star}}{R_{\odot}} \right)^3. \quad (4.1)$$

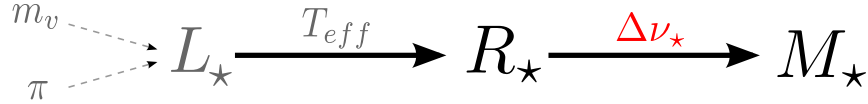


Figure 4.7.: Procedure B - Processing diagram to derive the 'classical' radius. The mass is computed using the seismic observable  $\Delta\nu$ .

### Procedure C - Asteroseismic radius constraint



Figure 4.8.: Procedure C - Processing diagram to derive the stellar radius and mass. This time all parameters are computed like in Procedure A, then the mass is combined with the large separation to calculate the radius.

In this approach the mass of the star is fixed to the classical value from Procedure

#### 4. Numerical experiment

A. The radius of the star is computed using Equation (2.12):

$$\frac{R_{\star}}{R_{\odot}} = \left( \frac{M_{\star}/M_{\odot}}{(\Delta\nu_{\star}/\Delta\nu_{\odot})^2} \right)^{1/3}. \quad (4.2)$$

#### Procedure D - Asteroseismic modeling

To reach the highest possible precision, I take the (modeled) asteroseismic values for the stellar mass and radius from the original publications (Batalha et al., 2011, Borucki et al., 2012, Howell et al., 2012). With these values I can check what will happen in comparison with procedure E.

#### Procedure E - Future possibilities: Gaia & PLATO

Finally I study the effects of planned future missions. I simulate the effects of the high precision radius determination of Gaia (Section 3.3.3), combined with the observation of brighter stars by PLATO (Section 3.3.3). Thus, I set the upper limit on the precision of the radius (due to Gaia) and mass (due to PLATO) to 2% and the precision on the RV semi-amplitude to 1 m/s (highest precision available with HIRES/Keck, Section 3.3.1).

#### 4.2.2. Exoplanet characteristics

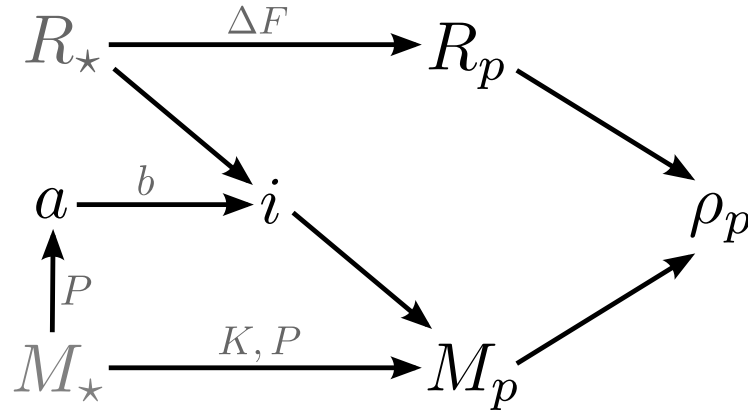


Figure 4.9.: Diagram for the calculation of planetary parameters down to the planetary density.

As described in Section 3.2.1, I use Equation (3.7) for the planetary semi-major axis, Equation (3.8) for its inclination and finally Equation (3.1) for the planetary

radius. From the combination with Doppler spectroscopy the exact exoplanet mass is deduced using Equation (3.10).

For characteristics concerning the habitability of the exoplanet I calculate the density using the planetary mass and radius. For the inner and outer boundary of the habitable zone I adopt Equation (3.11). The surface temperature of the exoplanet can also be constrained with Equation (3.11), rearranged for  $T_{\text{eq}}$  and using the corresponding semi-major axis for the planet (see Section 3.2.3 for details).





## 5. Results and discussion

In the following sections I present the results of my work. The shown plots and histograms are always for the Kepler-21 system, its values are listed in Appendix A. The corresponding figures, as well as a complete summary of the most important resulting parameters for Kepler-10 and Kepler-22 can be seen in the Appendices B and C.

### 5.1. Validation and systematics

As announced in Section 4.2.1 I investigate the deviation of my calculations from the published parameters for the stellar and planetary radius and mass of the three program stars. Hence, I use the different methods described in Section 4.2 and compare the results for each parameter and procedure with the reference values published by Howell et al. (2012) for K-21 (Kepler-21), Batalha et al. (2011) for K-10 (Kepler-10) and Borucki et al. (2012) for K-22 (Kepler-22).

The parameters obtained with the various methods are listed in Tables A.1, B.1 and C.1. Figure 5.1 shows the results with corresponding uncertainties compared to the reference values for K-21.

I find that the absolute values for stellar and planetary radius and mass are in good agreement and match the reference values. For stellar radius and mass the deviation of my values to the referenced ones are not smaller than the standard deviation of the reference. But compared to the corresponding errors the deviation from the reference values is only marginal. For K-21 the stellar radii for procedures A, B and C are nearly located within the  $1\text{-}\sigma$ -range. The mass estimates are clearly outside, but the deviations are small. Additionally the seismic  $1\text{-}\sigma$ -range of the reference is much smaller than the ones for A, B and C. For the planetary parameters the absolute values come closer to the reference and for K-21 the planetary radius is within the error range of the reference. The planetary mass estimates are really close to the one of Howell et al. (2012).

## 5. Results and discussion

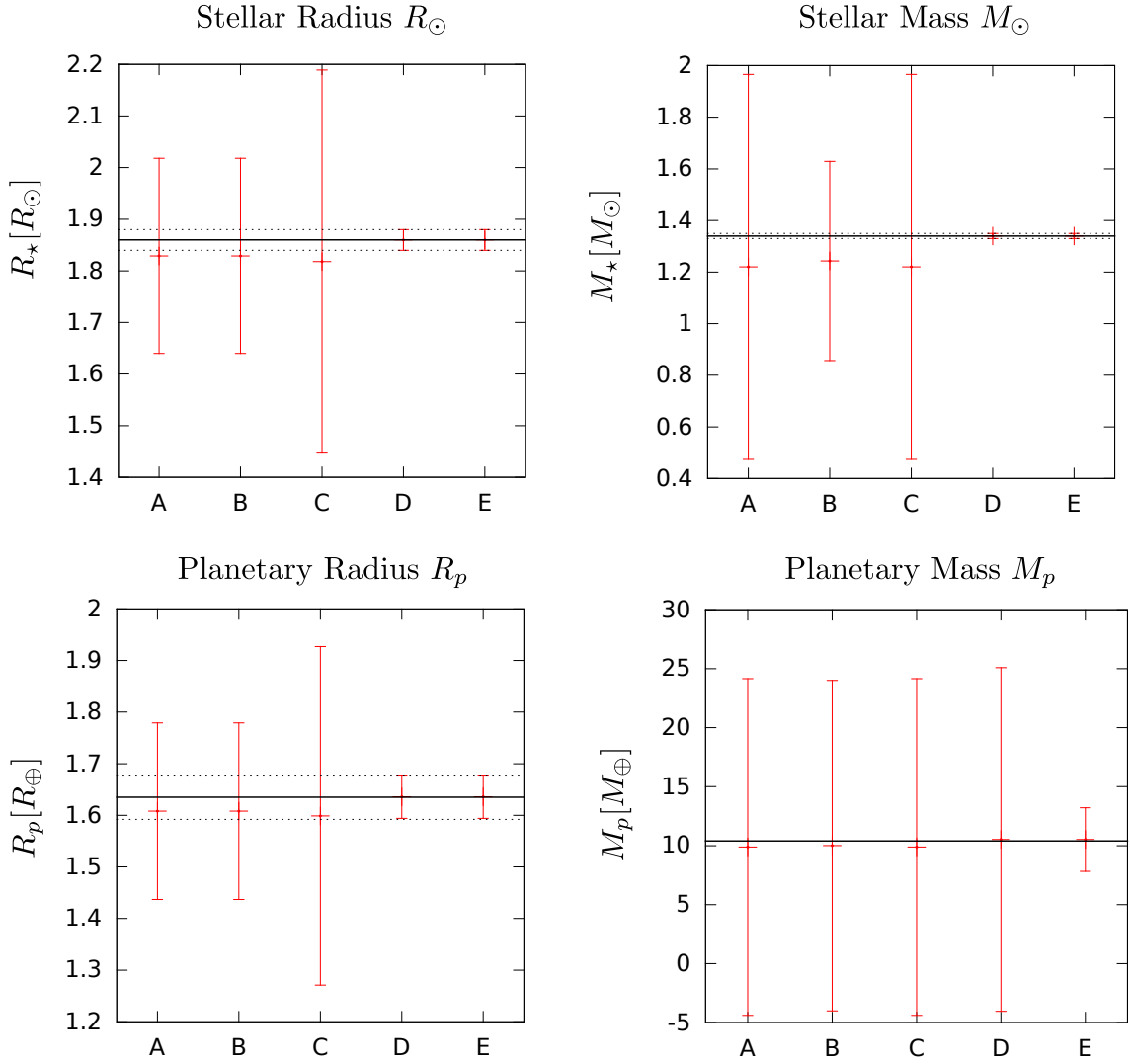


Figure 5.1.: Validation of the numerical methods for Kepler-21. The solid black lines show the reference value for each parameter, the dotted lines indicate the corresponding 1- $\sigma$  error range. Plotted are the parameters for stellar and planetary radius and mass for each procedure. The errors show the quality of the specific estimate. For the planetary mass the absolute value is just a rough estimate and Howell et al. (2012) don't state a specific uncertainty. All reference values are from Howell et al. (2012).

Because the planetary radius and mass are the two most crucial parameters of my study I rearranged the results for the validation in Figure 5.2. This plot tells how the set of parameters changes compared to the set of corresponding errors. The plots for all systems (K-10 and K-22 are given in Appendix B and C) reveal that the displacement in values is small compared to the change in uncertainty and that the errors tend to decrease from Procedure A to E in general.

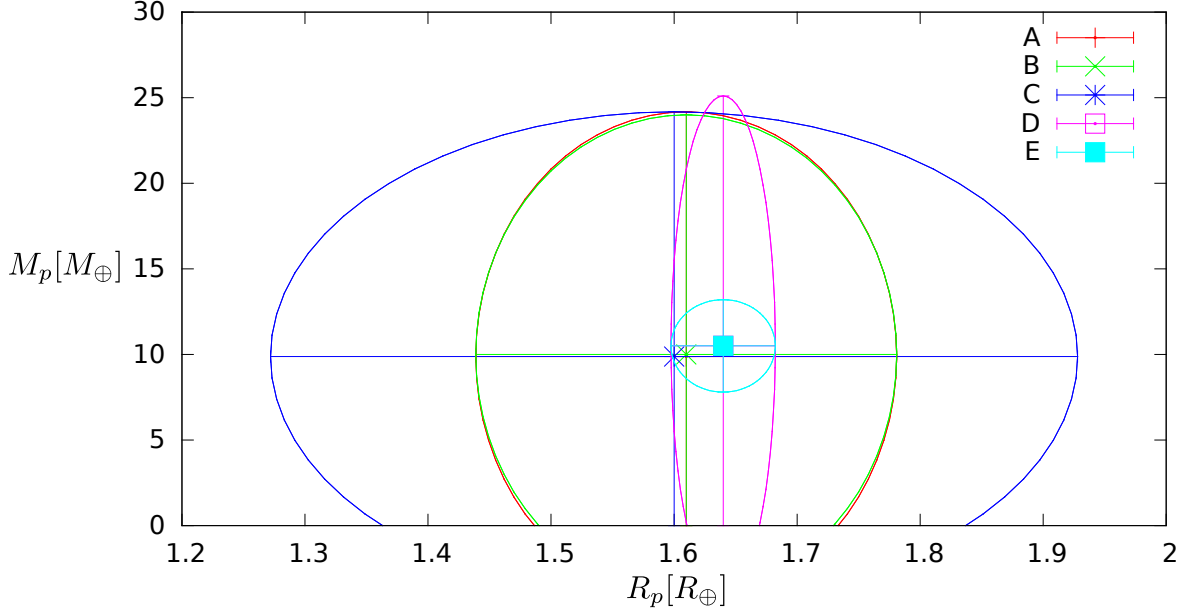


Figure 5.2.: Planetary radius vs. mass for all procedures of Kepler-21b with corresponding areas of 1 standard deviation (ellipses). The uncertainties tend to decrease from Procedure A/B to D and E. The increase for the radius error in Procedure C will be discussed in Section 5.3.3.

Regarding the strong uncertainties in Procedures A, B and C I think that my code produces values really close to the referenced ones. Therefore the displacement in the absolute values don't show strong influences in the propagation of errors. This means I can fix the stellar parameters to the seismic values from the publications and the relative differences in the computed errors are affected only marginal. Under this assumption it will be easier to compare the real effects of the procedures on the change in planetary uncertainties because the values of stellar mass and radius don't inflict the derivative terms in the propagation of errors.

## 5.2. Constraints on stellar characteristics

### 5.2.1. Stellar radius

The uncertainty of the radius estimate for the different methods and three program stars is shown in Figure 5.3. The crucial procedure in this estimate is C, where I insert the constraint from Equation (2.12).

It is important to note that this procedure somehow spins round: At first I com-

## 5. Results and discussion

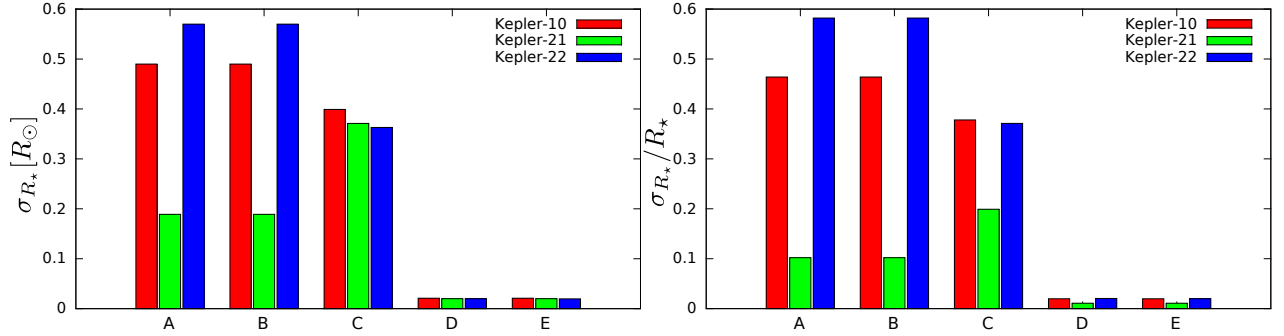


Figure 5.3.: Error in stellar radius  $R_*$  for all systems and procedures. The left panel shows the error in units of solar radii  $R_\odot$ , the right panel illustrates the relative error  $\sigma_{R_*}/R_*$ . The values for K-21 in the right hand panel in Procedure D and E are below 0.02, because the estimate for this value from seismic modeling in Procedure D is already below this value and is therefore not set to 0.02 for Procedure E.

pute a classical estimate for stellar mass from the classical stellar radius and then combine it with the large separation to induce a ‘seismic’ constraint. Therefore the uncertainty for the ‘seismic’ stellar radius is directly affected by the uncertainty estimate for the classical stellar radius and especially the stellar mass. As I will show in Section 5.2.2 the precision of  $M_*$  is quite bad and this dependency influences the determination of the error in stellar radius in Procedure C.

Remarkably the errors go down for K-10 and K-22 in Procedure C and the one for K-21 does not. This is due to the chosen errors in stellar radius for the K-10 and K-22 systems in Procedure A and B, which I guessed using estimates from Verner et al. (2011) and Valenti & Fischer (2005) (see Section 4.1.2). These estimates are quite pessimistic and as it can be seen from K-21 the errors would be smaller with available parallaxes. Thus, the errors for Procedure A and B (where the values are the same) for K-10 and K-22 are worse, even if the estimate for Procedure C, influenced by the large uncertainty in stellar mass, is quite bad as well.

In contrast, for K-21 I compute the radius error myself, receive smaller estimates in Procedure A/B and hence, the error is worse in Procedure C, due to the dependency on the error in stellar mass. Figure 5.4 shows the variance of the stellar radius for K-21, including the dependencies from basic input parameters. This clearly shows, that from Procedure A to Procedure C the change in variance (and hence uncertainty) is due to the contribution of the mass error, which is mainly dominated by the error in  $\log g_*$ .

For all three systems the step from Procedures A/B to Procedure D and E is

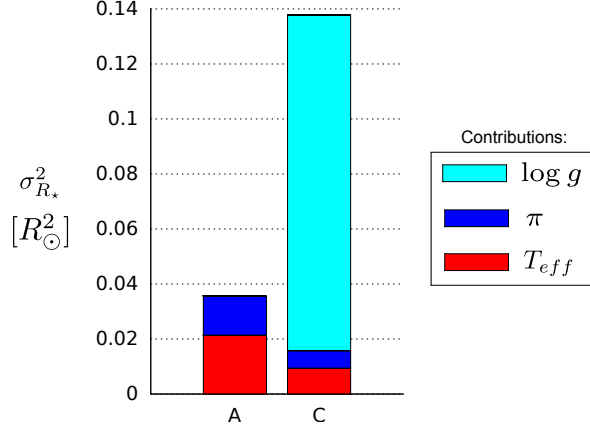


Figure 5.4.: Variance of  $R_\star$  for Kepler-21 and Procedure A, B, respective C. The different colors indicate the contributions from the propagated errors of various parameters used for the calculation.

really huge. The modeling and future scenario boost the precision by a factor of 10 for K-21 and even 20 for K-10 and K-22. However, it is possible that in the modeling case for the Kepler systems there can exist some systematic errors, which are not weighted and named in the publications and consequently not included in my calculation.

### 5.2.2. Stellar mass

Figure 5.5 illustrates the absolute and relative uncertainties in stellar mass for all procedures. As for the radius, the expected improvement of Procedure B works fine for two systems, this time for K-10 and K-21. In contrast, the mass uncertainty gets worse for K-22. To get an idea what happens, I look at the error propagation terms and compare the formulas used in procedure A and B:

$$\sigma_{M_\star}(A) = \sqrt{\sigma_{\log g_\star}^2 (R_\star^2 10^{\log g_\star} \log(10))^2 + \sigma_{R_\star}^2 (2R_\star 10^{\log g_\star})^2}, \quad (5.1)$$

$$\sigma_{M_\star}(B) = \sqrt{\sigma_{\Delta\nu_\star}^2 (2\Delta\nu_\star R_\star^3)^2 + \sigma_{R_\star}^2 (3\Delta\nu_\star R_\star^2)^2}. \quad (5.2)$$

In both formulas the contributions from the uncertainty in  $R_\star$  (second terms under the square root) are dominant. This term depends mainly on the absolute values for the large separation and the radius of the star. This explains, why the uncertainty increases for K-22. In this system both of these parameters are bigger compared to K-10, hence the error increases for K-22. For K-21 the large separation and the uncertainty in stellar radius are very small, which rules out the large absolute value

## 5. Results and discussion

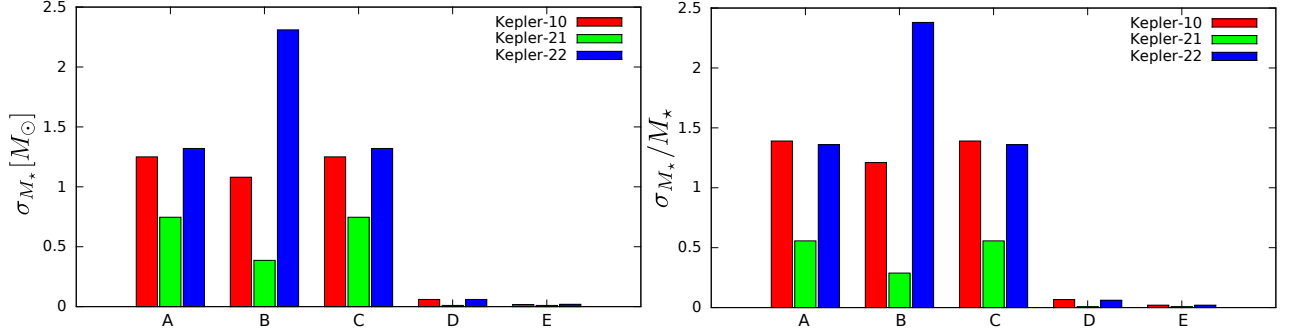


Figure 5.5.: Error in  $M_*$  for all systems and procedures. On the left side we can see the error in total units of  $M_\odot$  and on the right side we see the relative error  $\sigma_M/M_*$ . As in Figure 5.4, the relative error for K-21 in Procedure E differs from 0.02, because the estimate in Procedure D is already below this limit.

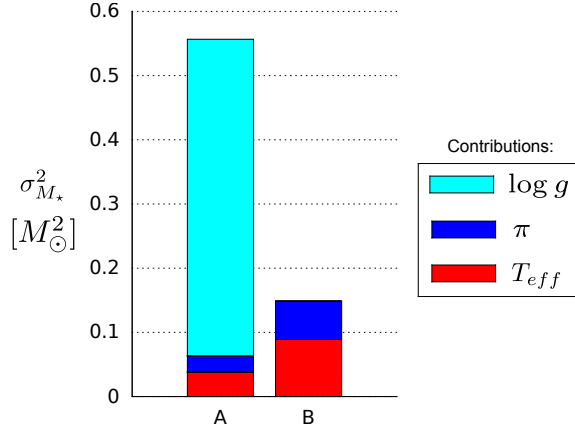


Figure 5.6.: Variance of  $M_*$  for Kepler-21 and Procedure A, B, respective C. The different colors indicate the contributions from the propagated errors of various parameters used for the calculation.

for  $R_*$ . Again, the precision achieves improvements of a factor  $\sim 15$  in Procedure D. For K-10 and K-22 Procedure E even shows improvements of the factor  $\sim 40 - 50$ , compared to A. For K-21 there is no improvement from D to E, because the estimates of K-21 from the seismic modeling are below 2%, therefore the precision does not change.

### 5.3. Constraints on exoplanet characteristics

Now I start with the exoplanet parameters. Note again that the plots shown here are from K-21. The ones for K-10 and K-22 can be seen in Appendices B and C.

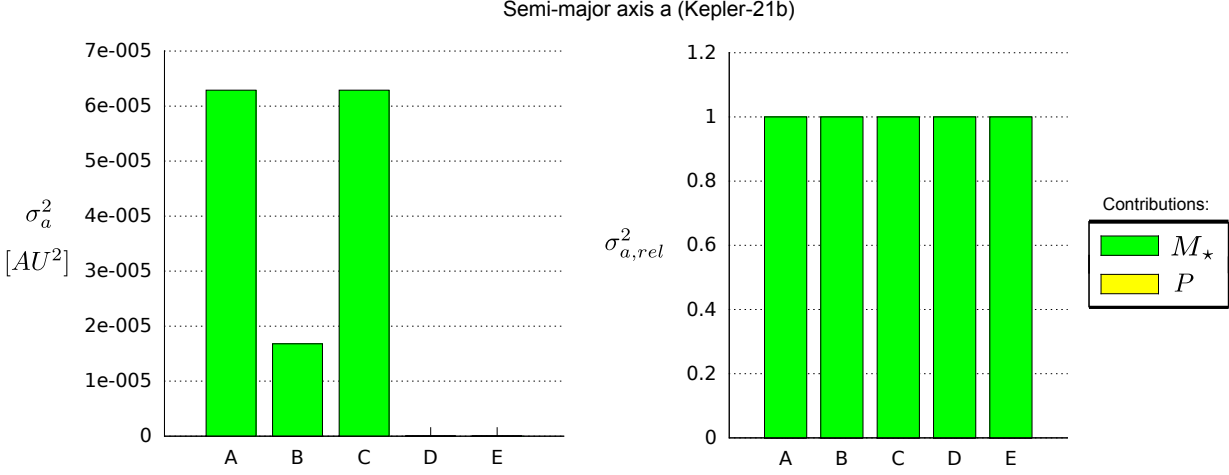


Figure 5.7.: Variance of  $a$  for all procedures of Kepler-21b. The left hand panel shows the total variance, the right hand panel shows the variance normalized to one. Green indicates contributions of  $M_*$ . Note that the contribution of the uncertainty of  $P$  is tiny, compared to the contribution of the mass uncertainty, such that it is not visible in the plots.

### 5.3.1. Planetary semi-major axis and inclination

The semi-major axis  $a$  of the planetary orbit is generally sensitive to the stellar mass and the orbital period, due to Kepler’s third law. However, the uncertainty in  $a$  is strongly dominated by the uncertainty in  $M_*$  (as shown in Figure 5.7) because the measurement of the orbital period is very precise.

The inclination of the systems is more interesting, according to Equation (3.8). It depends strongly on the uncertainties of both the stellar radius and the mass (through the semi-major axis  $a$ ).

In K-21 the improvement in stellar mass for Procedure B leads to higher precision, whereas the high uncertainty for the inclination in Procedure C can be explained with the high error in  $R_*$ . In K-10 the uncertainty in inclination goes down from Procedure A to C, as a result of the generally decreasing errors for stellar radius and mass. Due to the dependency on the uncertainty of  $M_*$  the uncertainty in inclination for K-22 increases in Procedure B and decreases in C.

The uncertainty in the impact parameter  $b$ , usually a free parameter of the modeling, doesn’t change its absolute value because I deal with it as a constant and take its values from the corresponding publications. Thus, for proper modeling (Procedure D and E) the uncertainty of the inclination is dominated by the uncertainty in the impact parameter.

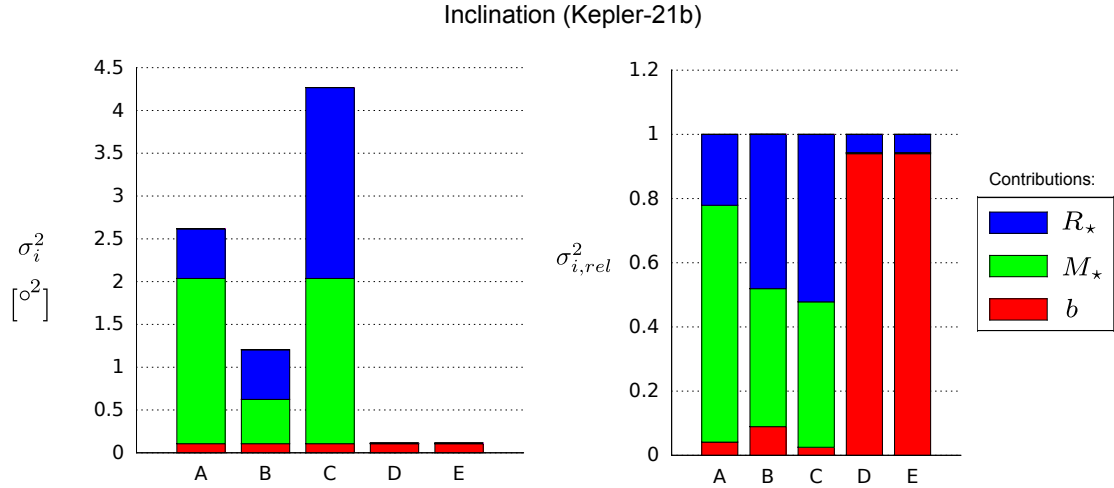


Figure 5.8.: Variance of  $i$  for all procedures of Kepler-21b. The left panel shows the contributions of individual parameters to the variance. The right panel shows the contributions normalized to one.

### 5.3.2. Planetary mass

Now I take a look at the two most crucial exoplanet parameters, the mass and radius. The uncertainties in planetary mass are calculated using Equation (3.10) and are therefore sensitive to the orbital period, the inclination, the RV semi-amplitude and the stellar mass.

In Figure 5.9 the error of the planet mass is dominated by the RV semi-amplitude  $K$  and little by the stellar mass  $M_*$ . Figure 5.9 could be misunderstood easily. The problem with this histogram is the correlation between  $M_*$  and  $K$ . For a full interpretation of the planet mass uncertainty I would have to investigate the correlation between those two parameters with a specific interest for the cross-correlations for the propagation of errors. Such an analysis is beyond the scope of this thesis. In the corresponding papers the values are gained independently and therefore I don't have further information. Hence I use the non-correlated gaussian distribution for the error, treating both variables independently.

Under this premise the most crucial aspect for getting a precise estimate for the mass is to make high-precision RV observations possible. Here Procedure E with Plato shows his full potential and I achieve a precision  $\sim 6$  times better than for Procedure A to D for K-21 and K-22. For K-10 the improvement of a factor  $\sim 4$  can already be seen in Procedure D, because its RV measurements are quite good.



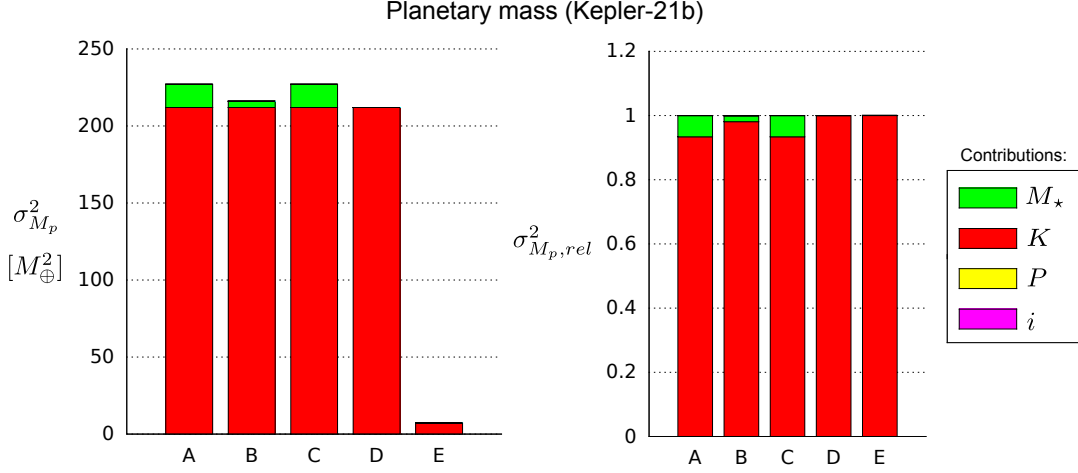


Figure 5.9.: Variance of  $M_p$  for all procedures of Kepler-21b. The left panel shows again the contributions to the variance for the various parameters, the right panel the variance normalized to one. The orbital period  $P$  and the inclination  $i$  are negligible compared to the stellar mass  $M_\star$  and the RV semi-amplitude  $K$  and can not be seen in the plot. The variance of  $K$  depends on the quality of the RV measurements, which leads to a huge improvement in Procedure E (PLATO case).

### 5.3.3. Planetary radius

The uncertainty of the radius is calculated using Equation (3.1) and shows the expected behaviour (see Figure 5.10). Due to the high precision of today's transit observations the exoplanet radius is mainly a function of the uncertainty in stellar radius. For Kepler-10b and Kepler-22b the seismic constraint in Procedure C works very well and I receive increased precision of a few percent. In contrast, for K-21 the precision decreases because of the increase in the error of the stellar radius (see Section 5.2.1).

The dependency of the uncertainty in the change of flux  $\Delta F$  becomes important in Procedures D and E, since I assume the same precision for PLATO as for Kepler observations. In these procedures the error is mainly a function of the uncertainty in transit depth and further refinements have to come from more accurate photometric measurements (which may be achievable with PLATO with the investigation of brighter stars and may change the exact relations, but is not included here). This shows again the strong influences of asteroseismic constraints of stellar parameters on the body parameter estimation for the exoplanets.

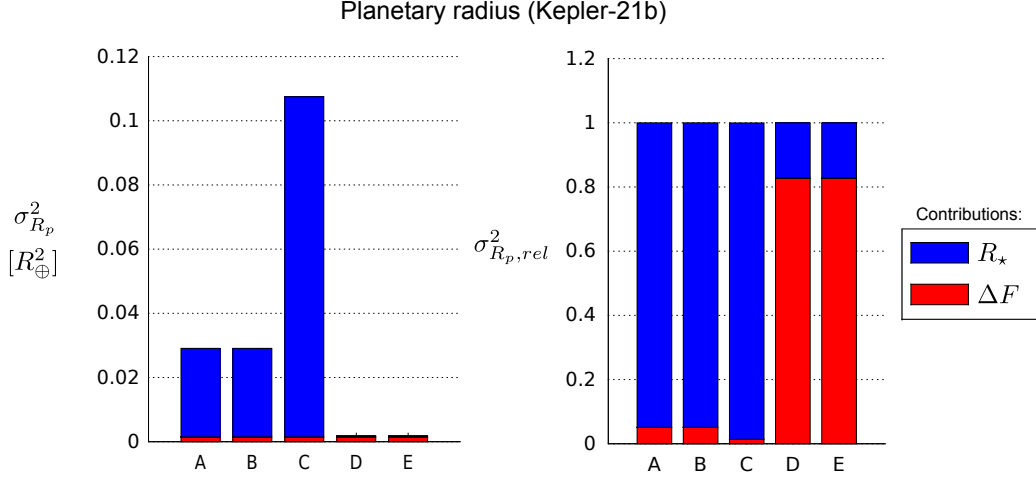


Figure 5.10.: Variance of  $R_p$  for all procedures of Kepler-21b. The left panel shows the contributions to the variance for the stellar radius and the transit depth, the right panel the variance normalized to one. The uncertainty in the estimation of the stellar radius dominates the uncertainty for the planetary radius, due to precise flux measurements of the corresponding stars.

#### 5.3.4. Planetary density

The density evaluation is illustrated in Figure 5.11 and shows the same trends as  $M_p$ , since the stellar mass  $M_*$  also affects the planet density  $\rho_p$  the most. The effect of the stellar radius  $R_*$  can be seen, but is small compared to the effect of the mass. Taking into account the strong influence of the RV measurements on  $M_*$  (see Section 5.3.2) it becomes obvious that also for the density the precision of the RV semi-amplitude  $K$  is the most important parameter. This is why the observation of brighter stars is extremely important for investigating the planetary interior.

#### 5.3.5. Habitable zone

The minimum ( $T_{eq} = 373K$ ) and maximum radii ( $T_{eq} = 273K$ ) of the HZ are computed using Equation (3.11) and the corresponding uncertainties are therefore dependent on the values for stellar radius and effective temperature. Its variances can be seen in Figure 5.12. The uncertainties for both the inner and outer boundary radii of the HZ are mainly dominated by the error of the stellar radius. Since the effective temperatures of K-10 and K-22 are better characterized than for K-21, the dependency on  $T_{eff}$  is negligible in these systems. As Procedure C in histogram 5.12 reveals, the HZ is very sensitive to increasing uncertainties in  $R_*$ , therefore the error

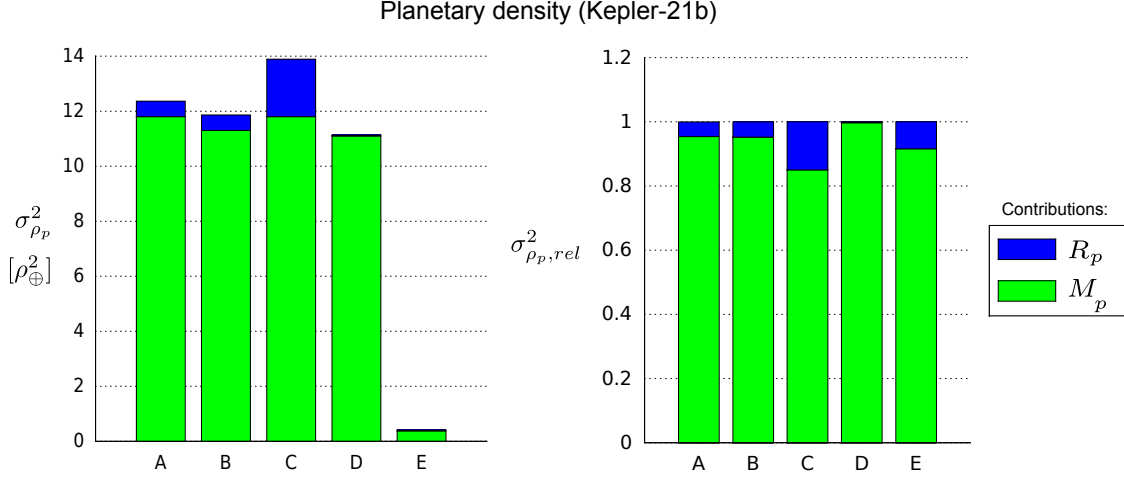


Figure 5.11.: Variance of  $\rho_p$  for all procedures of Kepler-21b. The left panel shows the contributions to the variance, the right panel the variance normalized to one. The uncertainty is dominated mainly by the contribution of the planetary mass. Thus, precise RV measurements are important to obtain informations about the planetary interior (see Section 5.3.2).

doubles for K-21, due to the growth of the stellar mass error in this Procedure (see Section 5.2.1).

### 5.3.6. Planetary surface temperature

Rearranging Equation (3.11), involving the planetary semi-major axis  $a$  as  $R_{\text{HZ}}$  and solving for  $T_{\text{eq}}$  I compute the planet surface temperatures and corresponding uncertainties. The uncertainty of the surface temperature is sensitive to the effective temperature of the host star, the stellar radius and the semi-major axis. The two last values dominate the errors. Taking Section 5.3.1 into account,  $a$  is dominated by the stellar mass, hence the precision of the planetary surface temperature is strongly correlated to both stellar values. For K-10 and K-22, the dependency on  $T_{\text{eff}}$  is again small, due to the high precision of this estimate.

## 5. Results and discussion

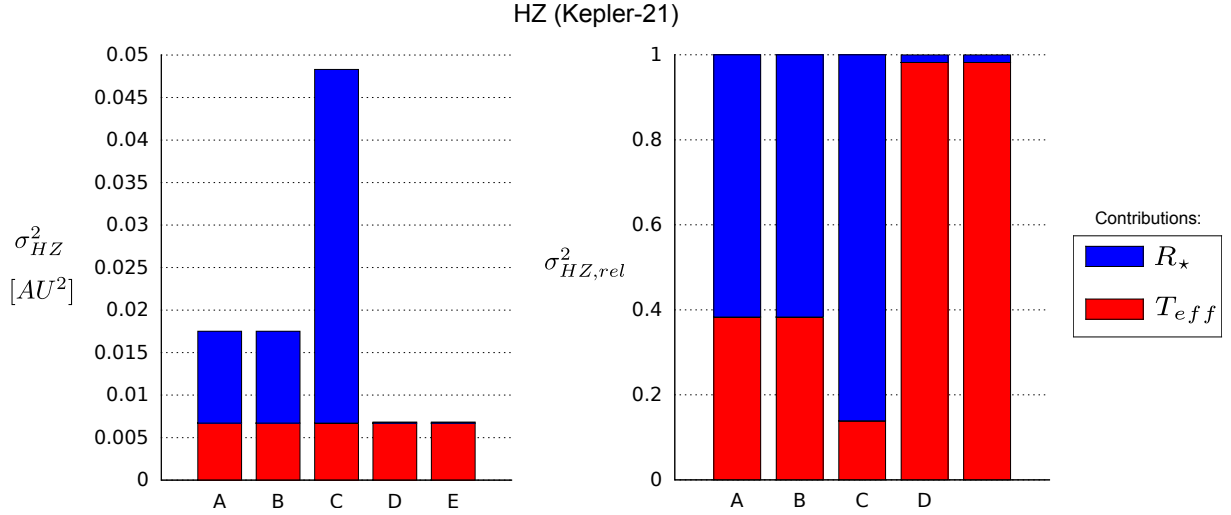


Figure 5.12.: Variance of inner and outer boundaries of the HZ for all procedures of Kepler-21b. The left panel shows the contributions to the variance, the right panel the variance normalized to one. The uncertainty is dominated mainly by the contributions of the stellar radius and effective temperature of the corresponding star. It is important to note that the variances, as well as the dependencies, are the same for inner and outer boundary. Just the absolute values differ.

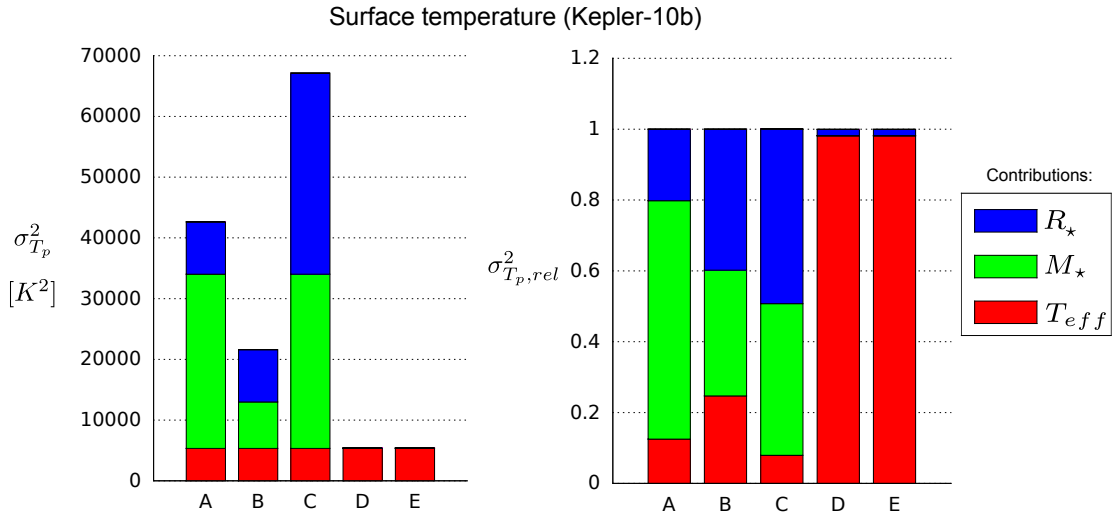


Figure 5.13.: Variance of surface temperature for all procedures of Kepler-21b. The left panel shows the contributions to the variance, the right panel the variance normalized to one. The uncertainty depends on the values for the radius, mass and the effective temperature of the host star.

## 6. Conclusions and summary

In this thesis I tested the dependence of the precision of exoplanet properties on the precision of the stellar radius and mass. I compared different computation methods, including 'classical' calculations, simple assumptions from asteroseismology, the results of state-of-the-art modeling presented in current papers and even assumptions on future possibilities with planned space missions.

Concerning the constraints for the stellar parameters I couldn't achieve high precisions on  $R_\star$  and  $M_\star$  with procedures A, B and C, i.e., classical methods and simple assumptions from asteroseismology. Especially for Procedures B and C where the AS density constraints are used, I expected higher precisions or improvements compared to Procedure A. Studying the results I conclude that if the quantities  $T_{\text{eff}}$ ,  $\log g$ ,  $m_v$  and  $\pi$  are precisely measured, good constraints on the stellar characteristics are possible. Generally the simple seismic assumptions from Procedure B and C can provide a rough idea on the parameters but they do not improve the precision on  $R_\star$  and  $M_\star$  significantly and are sometimes even less precise (e.g., the stellar radius in Procedure C for K-21).

The propagation of the uncertainties from the stars to the planets works quite well and the trends for the stellar parameters affect the uncertainties in the planetary errors, i.e., the uncertainties of planetary parameters show correct behaviours according to their dependency on the stellar characteristics. Generally the accuracies improve from Procedure A to D and E. In Procedures B and C there are some anomalies, which are explained in the corresponding paragraphs of Section 5.3.

Concerning the semi-major axis and the inclination of the exoplanets I reach very high precisions with errors down to  $< 1\%$  for Procedures D and E. The relative uncertainties for  $a$  and  $i$  in Procedures A, B and C are really good, compared to other planet parameters like mass or radius in this procedure, but they can even be improved by using the modeling (D) and future (E) methods. Regarding the semi-major axis it is important to note that I assume circular orbits, hence I can't be sure on the correct values regarding possible eccentricities. Nevertheless the errors in  $a$

## 6. Conclusions and summary

and  $i$  are satisfactory and with these it would be possible to derive tight constraints on celestial astronomy in exoplanetary systems.

The planetary radius can be constrained quite well and the precision improves a lot from Procedure A to D and E. Procedure C produces a bit odd results, which is explained in Section 5.2.1. The error is dominated by the error in stellar radius and I showed that improvements can be expected from seismic constraints.

The mass and density constraints don't work well with procedures A, B and C. The relative uncertainties are quite big. The limiting factor in the determination of the planet mass and density is the precision of the RV measurements. Significant improvements are expected by the observation of brighter stars, for instance with PLATO.

Overall I clearly proved the high value of proper asteroseismic modeling, all parameters benefit this way. Especially the precise estimates on the radius and the mass of the exoplanet in procedure D and E allow a good characterisation of the planetary system. Procedure E demonstrates impressively how missions like Gaia and PLATO may allow us to characterize exoplanet systems in the future.

### Prospects

In this last section I introduce some future possibilities, which may be achieved with high precision data. This summary isn't meant to be complete but it shows some extremely interesting aspects of future exoplanet science, which couldn't be included in this thesis.

Concerning the planetary body itself we have seen so far, that the it is possible to obtain very accurate estimates on mass and radius with AS constraints, which will allow us to distinguish different bulk compositions and structures, e.g., for the core, mantle and crust for rocky planets or gas envelope for giant planets. Figure 6.1 shows a scheme for compositions and the positions of known exoplanets in it.

Modeling the composition and the interior structure of terrestrial planets requires postulating reasonable assumptions about their composition. For better constrained masses and radii we can then model the planetary interior, which is directly linked to geophysical processes, e.g., convection, tectonics and magnetic field generation. Those have strong influence on the planetary conditions concerning habitability on rocky planets.

Figure 6.2 shows the link between the core-mantle ratio and possible convection

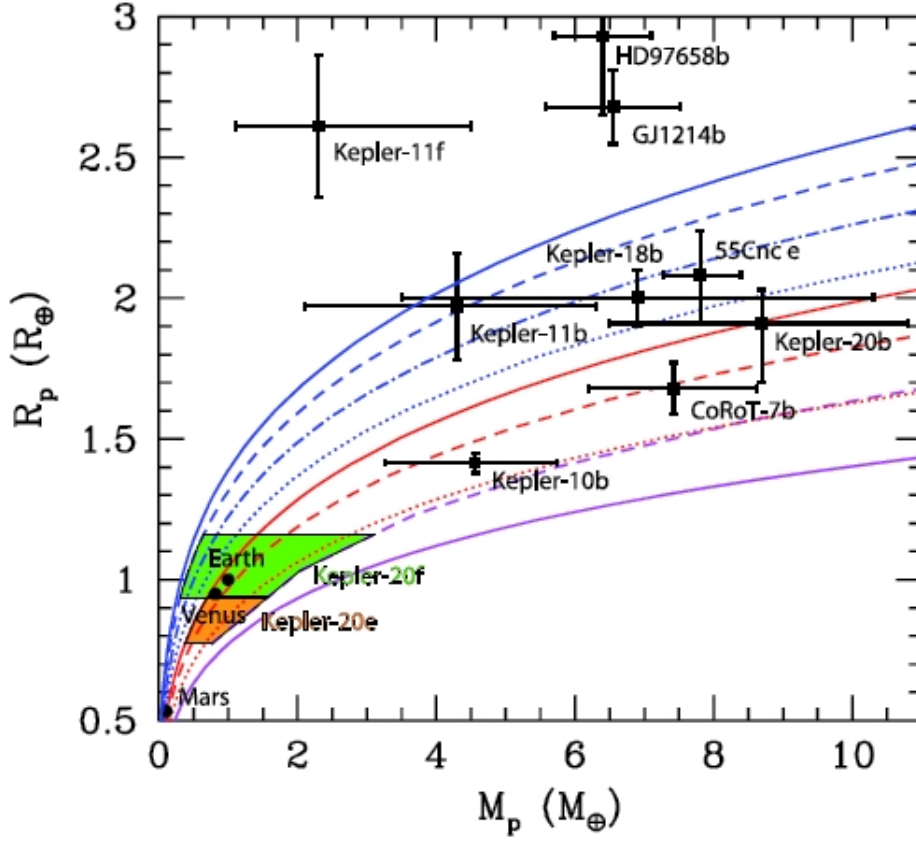


Figure 6.1.: Fressin et al. (2011) - Mass-radius diagram for various planets. The colored lines denote different compositions: water ice (blue), rocky (red) and iron (magenta). The orange and green areas mark the parameter range for Kepler 20 e and f.

patterns in the mantle of an exoplanet, which affects the outgassing and recycling of volatiles on planets with an earth-like atmosphere and is therefore important for stable conditions to facilitate possible extraterrestrial life.

With the help of asteroseismology it will be possible to test current planetary formation theories. For example, as stated in Section 2.2.4, it is possible to estimate a precise seismic age for the host star, which directly constrains the age of the associated planet. Comparing the inclination of the planet orbit (known from the transit measurement) and the inclination of the stellar rotation axis (known from asteroseismology, e.g., Gizon & Solanki, 2003) may allow to test different formation scenarios of exoplanet systems.

By obtaining a broad characterization of exoplanet and stellar parameters for many systems, e.g., mass, radius, gravitational acceleration, atmospheres and age,

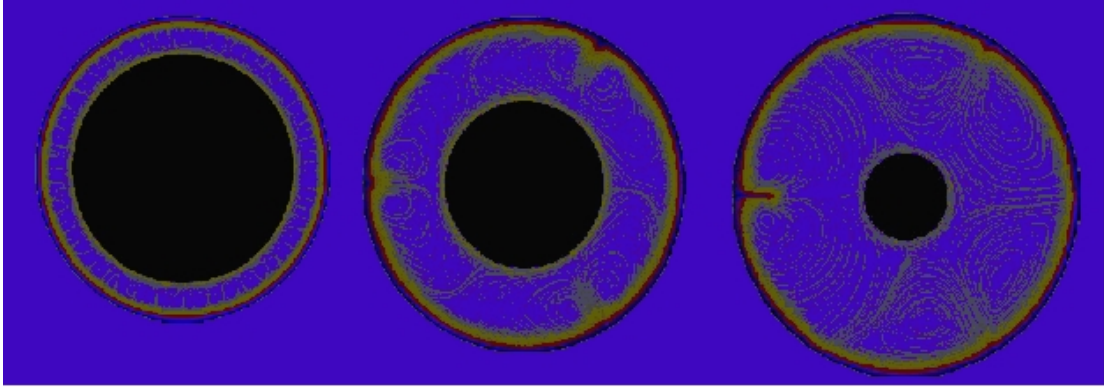


Figure 6.2.: Courtesy of L. Noack, D. Breuer (DLR) - Illustration of Earth-mass planets with different core-mantle ratio and possible mantle convection patterns. All three examples fit the same radius within  $\pm 5\%$  accuracy and can therefore not be distinguished without improved measurements.

it will even be possible to gain statistical conclusions.

All these constraints on planetary parameters are only achievable with tight constraints on the exoplanet's mass. To achieve such high precision it will be necessary to improve the RV resolution to its best accuracy. This is possible by observing brighter stars as it is planned with the PLATO spacecraft, which is a candidate for an ESA M-class mission and is considered for a possible launch around 2022. As indicated by Procedure E of my work PLATO would lift exoplanet science to the next level. Together with Gaia, which is planned to be launched in 2013, future observations will improve human's insight in this exciting new research area and we will possibly be able to classify our own solar system and the Earth in the Universe's evolution.



# A. Tables for Kepler-21b

Table A.1.: Resulting parameters for Kepler-21b. Values below the single lines indicate the contributions to the variance of the corresponding parameter.

<b>K-21 Parameter</b>	<b>A</b>	<b>B</b>	<b>C</b>	<b>D</b>	<b>E</b>
$R_{\star} [R_{\odot}]$	1.86E+00	1.86E+00	1.86E+00	1.86E+00	1.86E+00
$\sigma_{R_{\star}} [R_{\odot}]$	1.89E-01	1.89E-01	3.71E-01	2.00E-02	2.00E-02
$T_{\text{eff},CL} [R_{\odot}^2]$	2.14E-02	2.14E-02	2.14E-02	-	-
$m_{v,CL} [R_{\odot}^2]$	2.30E-06	2.30E-06	2.30E-06	-	-
$\pi_{CL} [R_{\odot}^2]$	1.43E-02	1.43E-02	1.43E-02	-	-
$\Delta\nu_{AS} [R_{\odot}^2]$	-	-	1.20E-04	-	-
$\log g_{\star,AS} [R_{\odot}^2]$	-	-	1.22E-01	-	-
$T_{\text{eff},AS} [R_{\odot}^2]$	-	-	9.40E-03	-	-
$m_{v,AS} [R_{\odot}^2]$	-	-	1.01E-06	-	-
$\pi_{AS} [R_{\odot}^2]$	-	-	6.29E-03	-	-
$M_{\star} [M_{\odot}]$	1.34E+00	1.34E+00	1.34E+00	1.34E+00	1.34E+00
$\sigma_{M_{\star}} [M_{\odot}]$	7.46E-01	3.86E-01	7.46E-01	1.00E-02	1.00E-02
$R_{\star,CL} [M_{\odot}^2]$	6.36E-02	-	6.36E-02	-	-
$\log g_{\star,CL} [M_{\odot}^2]$	4.93E-01	-	4.93E-01	-	-
$\Delta\nu_{AS} [M_{\odot}^2]$	-	1.51E-04	-	-	-
$T_{\text{eff},AS} [M_{\odot}^2]$	-	8.89E-02	-	-	-
$m_{v,AS} [M_{\odot}^2]$	-	9.55E-06	-	-	-
$\pi_{AS} [M_{\odot}^2]$	-	5.95E-02	-	-	-
$a [AU]$	4.27E-02	4.27E-02	4.27E-02	4.27E-02	4.27E-02
$\sigma_a [AU]$	7.93E-03	4.10E-03	7.93E-03	1.06E-04	1.06E-04
$\sigma_a/a$	1.86E-01	9.59E-02	1.86E-01	2.49E-03	2.49E-03
$P [AU^2]$	1.21E-13	1.21E-13	1.21E-13	1.21E-13	1.21E-13
$M_{\star} [AU^2]$	6.29E-05	1.68E-05	6.29E-05	1.13E-08	1.13E-08

Table A.1.: Resulting parameters for Kepler-21b. Values below the single lines indicate the contributions to the variance of the corresponding parameter.

<b>K-21 Parameter</b>	<b>A</b>	<b>B</b>	<b>C</b>	<b>D</b>	<b>E</b>
$i [^\circ]$	8.26E+01	8.26E+01	8.26E+01	8.26E+01	8.26E+01
$\sigma_i [^\circ]$	1.62E+00	1.10E+00	2.07E+00	3.38E-01	3.38E-01
$\sigma_i/i$	1.96E-02	1.33E-02	2.50E-02	4.09E-03	4.09E-03
$b [^\circ^2]$	1.07E-01	1.07E-01	1.07E-01	1.07E-01	1.07E-01
$R_\star [^\circ^2]$	5.80E-01	5.80E-01	2.23E+00	6.49E-03	6.49E-03
$P [^\circ^2]$	3.72E-09	3.72E-09	3.72E-09	3.72E-09	3.72E-09
$M_\star [^\circ^2]$	1.93E+00	5.17E-01	1.93E+00	3.47E-04	3.47E-04
$M_p [M_\oplus]$	1.05E+01	1.05E+01	1.05E+01	1.05E+01	1.05E+01
$\sigma_{M_p} [M_\oplus]$	1.51E+01	1.47E+01	1.51E+01	1.46E+01	2.70E+00
$\sigma_{M_p}/M_p$	1.43E+00	1.40E+00	1.43E+00	1.38E+00	2.56E-01
$K [M_\oplus^2]$	2.12E+02	2.12E+02	2.12E+02	2.12E+02	7.27E+00
$P [M_\oplus^2]$	1.71E-09	1.71E-09	1.71E-09	1.71E-09	1.71E-09
$M_\star [M_\oplus^2]$	1.50E+01	4.01E+00	1.50E+01	2.69E-03	2.69E-03
$R_\star [M_\oplus^2]$	3.34E-04	3.34E-04	1.28E-03	3.74E-06	3.74E-06
$b [M_\oplus^2]$	6.19E-05	6.19E-05	6.19E-05	6.19E-05	6.19E-05
$R_p [R_\oplus]$	1.64E+00	1.64E+00	1.64E+00	1.64E+00	1.64E+00
$\sigma_{R_p} [R_\oplus]$	1.71E-01	1.71E-01	3.28E-01	4.24E-02	4.24E-02
$\sigma_{R_p}/R_p$	1.04E-01	1.04E-01	2.01E-01	2.59E-02	2.59E-02
$R_\star [R_\oplus^2]$	2.76E-02	2.76E-02	1.06E-01	3.09E-04	3.09E-04
$M_\star [M_\oplus^2]$	1.49E-03	1.49E-03	1.49E-03	1.49E-03	1.49E-03
$\rho_p [\rho_\oplus]$	2.40E+00	2.40E+00	2.40E+00	2.40E+00	2.40E+00
$\sigma_{\rho_p} [\rho_\oplus]$	3.52E+00	3.44E+00	3.73E+00	3.33E+00	6.44E-01
$\sigma_{\rho_p}/\rho_p$	1.47E+00	1.43E+00	1.55E+00	1.39E+00	2.68E-01
$M_p [\rho_\oplus^2]$	1.18E+01	1.13E+01	1.18E+01	1.11E+01	3.80E-01
$R_p [\rho_\oplus^2]$	5.65E-01	5.65E-01	2.09E+00	3.49E-02	3.49E-02
$HZ_{\text{inner}} [AU]$	1.02E+00	1.02E+00	1.02E+00	1.02E+00	1.02E+00
$\sigma_{HZ_{\text{inner}}} [AU]$	1.32E-01	1.32E-01	2.20E-01	8.26E-02	8.26E-02
$\sigma_{HZ_{\text{inner}}}/HZ_{\text{inner}}$	1.29E-01	1.29E-01	2.15E-01	8.07E-02	8.07E-02
$R_\star [AU^2]$	1.08E-02	1.08E-02	4.16E-02	1.21E-04	1.21E-04
$T_{\text{eff}} [AU^2]$	6.71E-03	6.71E-03	6.71E-03	6.71E-03	6.71E-03

Table A.1.: Resulting parameters for Kepler-21b. Values below the single lines indicate the contributions to the variance of the corresponding parameter.

<b>K-21 Parameter</b>	<b>A</b>	<b>B</b>	<b>C</b>	<b>D</b>	<b>E</b>
$HZ_{\text{outer}} [AU]$	1.91E+00	1.91E+00	1.91E+00	1.91E+00	1.91E+00
$\sigma_{HZ_{\text{outer}}} [AU]$	2.47E-01	2.47E-01	4.10E-01	1.54E-01	1.54E-01
$\sigma_{HZ_{\text{outer}}}/HZ_{\text{outer}}$	1.29E-01	1.29E-01	2.15E-01	8.07E-02	8.07E-02
$R_{\star} [AU^2]$	3.77E-02	3.77E-02	1.45E-01	4.22E-04	4.22E-04
$T_{\text{eff}} [AU^2]$	2.34E-02	2.34E-02	2.34E-02	2.34E-02	2.34E-02
$T_{\text{surface}} [K]$	1.83E+03	1.83E+03	1.83E+03	1.83E+03	1.83E+03
$\sigma_{T_{\text{surface}}} [K]$	2.07E+02	1.47E+02	2.59E+02	7.37E+01	7.37E+01
$\sigma_{T_{\text{surface}}}/T_{\text{surface}}$	1.13E-01	8.05E-02	1.42E-01	4.04E-02	4.04E-02
$R_{\star} [K^2]$	8.61E+03	8.61E+03	3.31E+07	9.64E+01	9.64E+01
$T_{\text{eff}} [K^2]$	5.33E+03	5.33E+03	5.33E+03	5.33E+03	5.33E+03
$P [K^2]$	5.52E-05	5.52E-05	5.52E-05	5.52E-05	5.52E-05
$M_{\star} [K^2]$	2.87E+07	7.66E+03	2.87E+07	5.16E+00	5.16E+00

Table A.2.: Validation of the numerical methods for the Kepler-21 system. The last two rows are dimensionless. Reference values from Howell et al. (2012).

Procedure		Value $x$	$\sigma_x$	$x - x_{\text{Ref.}}$	$\sigma_x/x$	$\frac{x-x_{\text{Ref.}}}{x_{\text{Ref.}}}$
$R_\star [R_\odot]$	Ref.	1.860	0.020	-	0.011	-
	A	1.829	0.189	-0.031	0.103	-0.017
	B	1.829	0.189	-0.031	0.103	-0.017
	C	1.818	0.371	-0.031	0.103	-0.017
	D	1.860	0.020	0.000	0.011	0.000
	E	1.860	0.020	-0.042	0.204	-0.023
$M_\star [M_\odot]$	Ref.	1.340	0.010	-	0.007	-
	A	1.220	0.746	-0.120	0.011	-0.089
	B	1.243	0.386	-0.097	0.311	-0.073
	C	1.220	0.746	-0.120	0.011	-0.089
	D	1.340	0.010	0.000	0.007	0.000
	E	1.340	0.010	0.000	0.612	0.000
$a_p [R_\star]$	Ref.	4.912	0.014	-	0.003	-
	A	4.867	1.113	-0.045	0.007	-0.009
	B	4.897	0.716	-0.015	0.146	-0.003
	C	4.897	1.412	-0.015	0.007	-0.003
	D	4.937	0.054	0.025	0.011	0.005
	E	4.937	0.054	0.025	0.288	0.005
$i_p [^\circ]$	Ref.	82.580	0.310	-	0.004	-
	A	82.445	1.769	-0.135	0.011	-0.002
	B	82.490	1.153	-0.090	0.014	-0.001
	C	82.490	2.203	-0.090	0.011	-0.001
	D	82.551	0.338	-0.029	0.004	0.000
	E	82.551	0.338	-0.029	0.027	0.000
$R_p [R_\oplus]$	Ref.	1.635	0.043	-	0.026	-
	A	1.608	0.171	-0.027	0.004	-0.017
	B	1.608	0.171	-0.027	0.106	-0.017
	C	1.599	0.328	-0.037	0.004	-0.022
	D	1.636	0.042	0.001	0.026	0.000
	E	1.636	0.042	0.001	0.026	0.000
$M_p [M_\oplus]$	Ref.	10.400	-	-	0.000	-
	A	9.885	14.268	-0.515	1.443	-0.050
	B	10.004	14.005	-0.396	1.400	-0.038
	C	9.884	14.267	-0.396	1.400	-0.038
	D	10.519	14.565	0.119	1.385	0.011
	E	10.519	2.698	-0.516	1.443	-0.050

## B. Tables and Figures for Kepler-10b

Table B.1.: Resulting parameters for Kepler-10b. Values below the single lines indicate the contributions to the variance of the corresponding parameter.

Kepler-10	A	B	C	D	E
$R_{\star} [R_{\odot}]$	1.06E+00	1.06E+00	1.06E+00	1.06E+00	1.06E+00
$\sigma_{R_{\star}} [R_{\odot}]$	4.90E-01	4.90E-01	3.99E-01	2.10E-02	2.10E-02
$\Delta\nu_{AS} [R_{\odot}^2]$	-	-	1.73E-06	-	-
$M_{\star,AS} [R_{\odot}^2]$	-	-	1.59E-01	-	-
$M_{\star} [M_{\odot}]$	8.95E-01	8.95E-01	8.95E-01	8.95E-01	8.95E-01
$\sigma_{M_{\star}} [M_{\odot}]$	1.25E+00	1.08E+00	1.25E+00	6.00E-02	1.79E-02
$R_{\star,CL} [M_{\odot}^2]$	1.48E+00	-	1.48E+00	-	-
$\log g_{\star,CL} [M_{\odot}^2]$	7.83E-02	-	7.83E-02	-	-
$\Delta\nu_{AS} [M_{\odot}^2]$	-	5.96E-06	-	-	-
$R_{\star,AS} [M_{\odot}^2]$	-	1.17E+00	-	-	-
$a [AU]$	1.68E-02	1.68E-02	1.68E-02	1.68E-02	1.68E-02
$\sigma_a [AU]$	7.78E-03	6.76E-03	7.78E-03	3.74E-04	1.12E-04
$\sigma_a/a$	4.64E-01	4.03E-01	4.64E-01	2.23E-02	6.67E-03
$P [AU^2]$	4.45E-15	4.45E-15	4.45E-15	4.45E-15	4.45E-15
$M_{\star} [AU^2]$	6.06E-05	4.56E-05	6.06E-05	1.40E-07	1.25E-08
$i [^{\circ}]$	8.43E+01	8.43E+01	8.43E+01	8.43E+01	8.43E+01
$\sigma_i [^{\circ}]$	3.99E+00	3.76E+00	3.68E+00	1.34E+00	1.34E+00
$\sigma_i/i$	4.73E-02	4.46E-02	4.36E-02	1.59E-02	1.59E-02
$b [^{\circ 2}]$	1.78E+00	1.78E+00	1.78E+00	1.78E+00	1.78E+00
$R_{\star} [^{\circ 2}]$	7.05E+00	7.05E+00	4.67E+00	1.30E-02	1.30E-02
$P [^{\circ 2}]$	5.19E-10	5.19E-10	5.19E-10	5.19E-10	5.19E-10
$M_{\star} [^{\circ 2}]$	7.07E+00	5.32E+00	7.07E+00	1.64E-02	1.46E-03
$M_p [M_{\oplus}]$	4.54E+00	4.54E+00	4.54E+00	4.54E+00	4.54E+00

Table B.1.: Resulting parameters for Kepler-10b. Values below the single lines indicate the contributions to the variance of the corresponding parameter.

<b>Kepler-10</b>	<b>A</b>	<b>B</b>	<b>C</b>	<b>D</b>	<b>E</b>
$\sigma_{M_p} [M_\oplus]$	4.42E+00	3.89E+00	4.42E+00	1.39E+00	1.38E+00
$\sigma_{M_p}/M_p$	9.73E-01	8.57E-01	9.73E-01	3.06E-01	3.03E-01
$K [M_\oplus^2]$	1.89E+00	1.89E+00	1.89E+00	1.89E+00	1.89E+00
$P [M_\oplus^2]$	7.84E-11	7.84E-11	7.84E-11	7.84E-11	7.84E-11
$M_\star [M_\oplus^2]$	1.76E+01	1.33E+01	1.76E+01	4.08E-02	3.63E-03
$R_\star [M_\oplus^2]$	4.42E-04	4.42E-04	2.93E-04	8.11E-07	8.11E-07
$b [M_\oplus^2]$	1.11E-04	1.11E-04	1.11E-04	1.11E-04	1.11E-04
$R_p [R_\oplus]$	1.42E+00	1.42E+00	1.42E+00	1.42E+00	1.42E+00
$\sigma_{R_p} [R_\oplus]$	6.59E-01	6.59E-01	5.37E-01	3.37E-02	3.37E-02
$\sigma_{R_p}/R_p$	4.64E-01	4.64E-01	3.78E-01	2.38E-02	2.38E-02
$R_\star [R_\oplus^2]$	4.34E-01	4.34E-01	2.88E-01	7.97E-04	7.97E-04
$M_\star [M_\oplus^2]$	3.40E-04	3.40E-04	3.40E-04	3.40E-04	3.40E-04
$\rho_p [\rho_\oplus]$	1.59E+00	1.59E+00	1.59E+00	1.59E+00	1.59E+00
$\sigma_{\rho_p} [\rho_\oplus]$	2.70E+00	2.59E+00	2.37E+00	4.99E-01	4.94E-01
$\sigma_{\rho_p}/\rho_p$	1.70E+00	1.64E+00	1.49E+00	3.14E-01	3.12E-01
$M_p [\rho_\oplus^2]$	2.38E+00	1.85E+00	2.38E+00	2.36E-01	2.32E-01
$R_p [\rho_\oplus^2]$	4.88E+00	4.88E+00	3.24E+00	1.28E-02	1.28E-02
$HZ_{\text{inner}} [AU]$	4.84E-01	4.84E-01	4.84E-01	4.84E-01	4.84E-01
$\sigma_{HZ_{\text{inner}}} [AU]$	2.26E-01	2.26E-01	1.85E-01	2.72E-02	2.72E-02
$\sigma_{HZ_{\text{inner}}}/HZ_{\text{inner}}$	4.67E-01	4.67E-01	3.81E-01	5.62E-02	5.62E-02
$R_\star [AU^2]$	5.05E-02	5.05E-02	3.34E-02	9.27E-05	9.27E-05
$T_{\text{eff}} [AU^2]$	6.48E-04	6.48E-04	6.48E-04	6.48E-04	6.48E-04
$HZ_{\text{outer}} [AU]$	9.04E-01	9.04E-01	9.04E-01	9.04E-01	9.04E-01
$\sigma_{HZ_{\text{outer}}} [AU]$	4.22E-01	4.22E-01	3.45E-01	5.08E-02	5.08E-02
$\sigma_{HZ_{\text{outer}}}/HZ_{\text{outer}}$	4.67E-01	4.67E-01	3.81E-01	5.62E-02	5.62E-02
$R_\star [AU^2]$	1.76E-01	1.76E-01	1.17E-01	3.23E-04	3.23E-04
$T_{\text{eff}} [AU^2]$	2.26E-03	2.26E-03	2.26E-03	2.26E-03	2.26E-03
$T_{\text{surface}} [K]$	2.00E+03	2.00E+03	2.00E+03	2.00E+03	2.00E+03
$\sigma_{T_{\text{surface}}} [K]$	6.60E+02	6.18E+02	6.02E+02	6.06E+01	5.68E+01
$\sigma_{T_{\text{surface}}}/T_{\text{surface}}$	3.29E-01	3.08E-01	3.00E-01	3.02E-02	2.83E-02

Table B.1.: Resulting parameters for Kepler-10b. Values below the single lines indicate the contributions to the variance of the corresponding parameter.

<b>Kepler-10</b>	<b>A</b>	<b>B</b>	<b>C</b>	<b>D</b>	<b>E</b>
$R_{\star} [K^2]$	2.16E+05	2.16E+05	1.43E+05	3.97E+02	3.97E+02
$T_{\text{eff}} [K^2]$	2.78E+03	2.78E+03	2.78E+03	2.78E+03	2.78E+03
$P [K^2]$	1.59E-05	1.59E-05	1.59E-05	1.59E-05	1.59E-05
$M_{\star} [K^2]$	2.17E+05	1.63E+05	2.17E+05	5.02E+02	4.47E+01

## B. Tables and Figures for Kepler-10b

Table B.2.: Validation of the numerical methods for the Kepler-10 system. The last two rows are dimensionless. Reference values from Batalha et al. (2011).

Procedure		Value $x$	$\sigma_x$	$x - x_{\text{Ref.}}$	$\sigma_x/x$	$\frac{x-x_{\text{Ref.}}}{x_{\text{Ref.}}}$
$R_\star [R_\odot]$	Ref.	1,056	0,021	-	1,989	-
	A	0.980	0.490	-0.076	0.500	-0.072
	B	0.980	0.490	-0.076	0.500	-0.072
	C	1.166	0.399	0.110	0.342	0.104
	D	1.056	0.021	0.000	0.020	0.000
	E	1.056	0.021	0.000	0.020	0.000
$M_\star [M_\odot]$	Ref.	0.895	0.060	-	0.067	-
	A	1.215	1.247	0.320	1.026	0.358
	B	0.722	1.082	-0.173	1.500	-0.194
	C	1.215	1.247	0.320	1.026	0.358
	D	0.895	0.060	0.000	0.067	0.000
	E	0.895	0.018	0.000	0.020	0.000
$a_p [R_\star]$	Ref.	3.436	0.092	-	0.027	-
	A	4.070	2.466	0.634	0.606	0.185
	B	3.421	2.419	-0.015	0.707	-0.004
	C	3.421	1.655	-0.015	0.484	-0.004
	D	3.411	0.102	-0.025	0.030	-0.007
	E	3.411	0.072	-0.025	0.021	-0.007
$i_p [^\circ]$	Ref.	84.400	0.079	-	0.001	-
	A	85.222	3.108	0.822	0.036	0.010
	B	84.313	4.248	-0.087	0.050	-0.001
	C	84.313	3.064	-0.087	0.036	-0.001
	D	84.296	1.345	-0.104	0.016	-0.001
	E	84.296	1.339	-0.104	0.016	-0.001
$R_p [R_\oplus]$	Ref.	1.416	0.036	-	0.025	-
	A	1.318	0.659	-0.098	0.500	-0.070
	B	1.318	0.659	-0.098	0.500	-0.070
	C	1.568	0.537	0.152	0.342	0.107
	D	1.420	0.034	0.004	0.024	0.003
	E	1.420	0.034	0.004	0.024	0.003
$M_p [M_\oplus]$	Ref.	4.560	1.290	-	0.283	-
	A	5.559	4.159	0.999	0.748	0.219
	B	3.932	4.109	-0.628	1.045	-0.138
	C	5.567	4.165	1.007	0.748	0.221
	D	4.540	1.391	-0.020	0.306	-0.004
	E	4.540	1.377	-0.020	0.303	-0.004



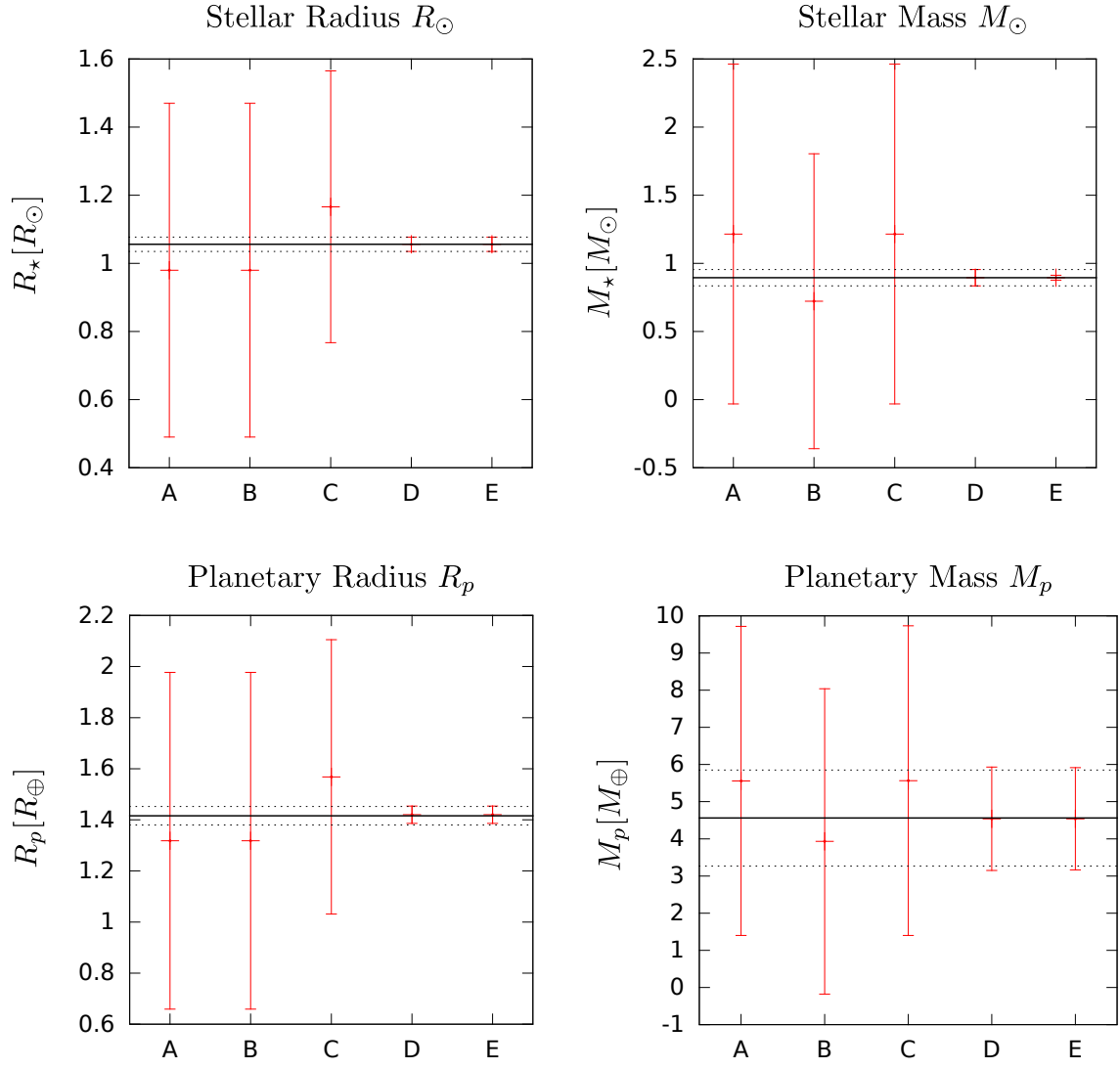


Figure B.1.: Validation of the numerical methods for Kepler-10. For a description see Figure 5.1. Reference values from Batalha et al. (2011).

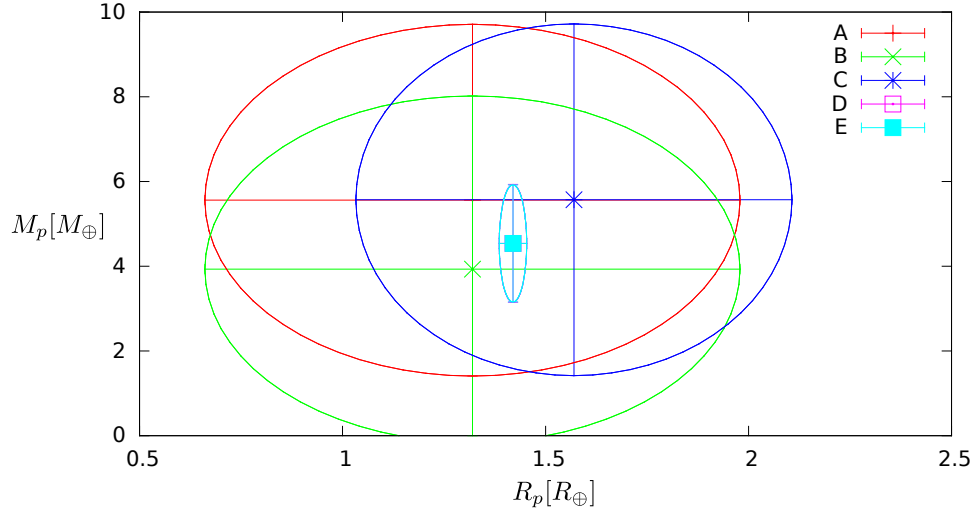


Figure B.2.: Planetary radius vs. mass for all procedures of Kepler-10b with corresponding areas of 1 standard deviation (ellipses).

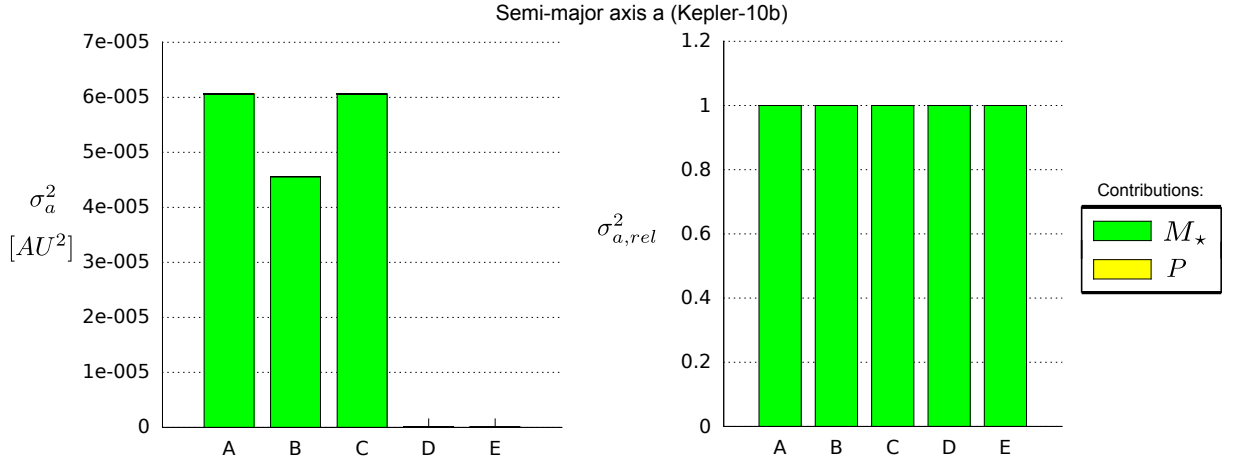


Figure B.3.: Variance of  $a$  for all procedures of Kepler-10b.

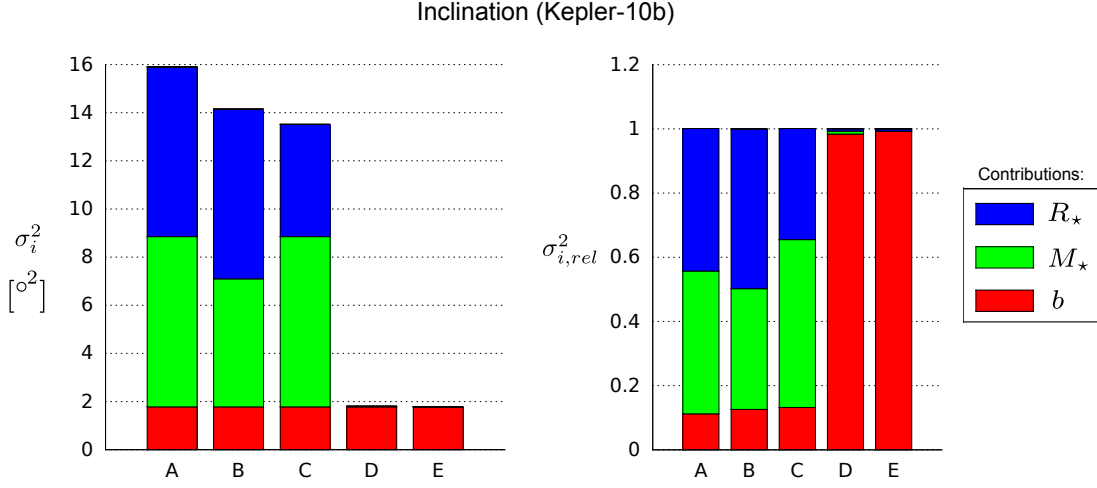


Figure B.4.: Variance of  $i$  for all procedures of Kepler-10b.

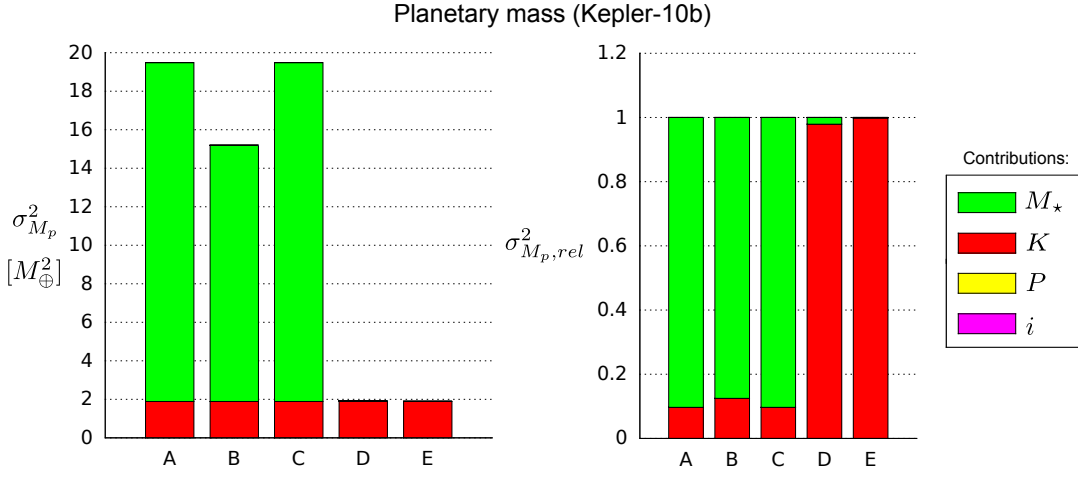


Figure B.5.: Variance of  $M_p$  for all procedures of Kepler-10b.

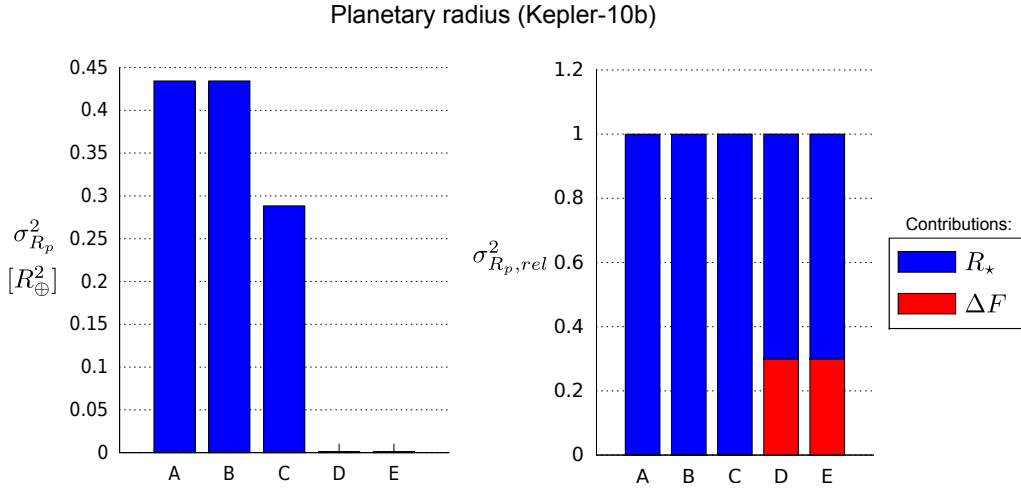


Figure B.6.: Variance of  $R_p$  for all procedures of Kepler-10b.

## B. Tables and Figures for Kepler-10b

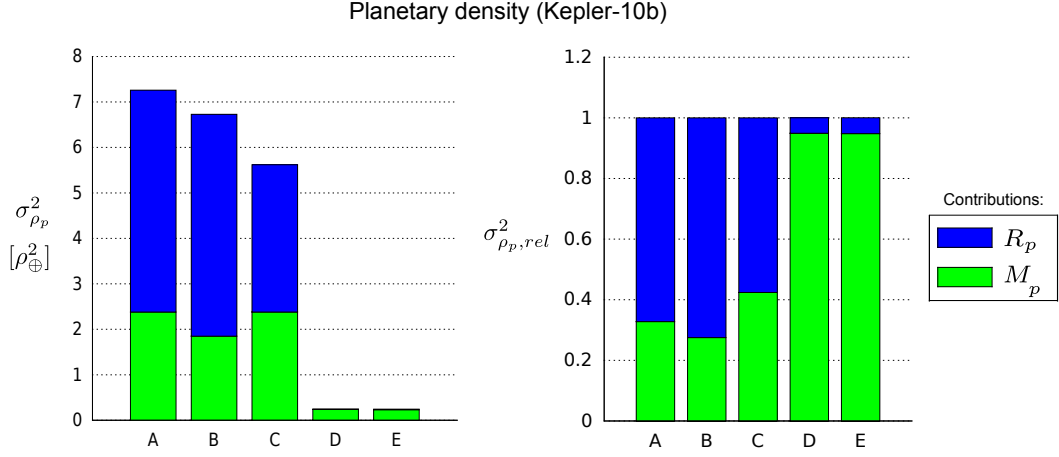


Figure B.7.: Variance of  $\rho_p$  for all procedures of Kepler-10b.

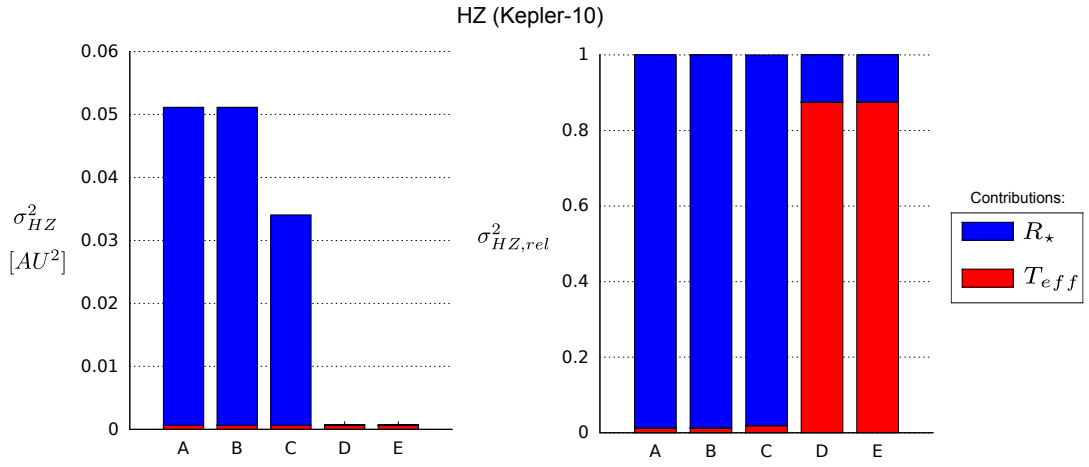


Figure B.8.: Variance of the boundaries of the HZ for all procedures of Kepler-10b.

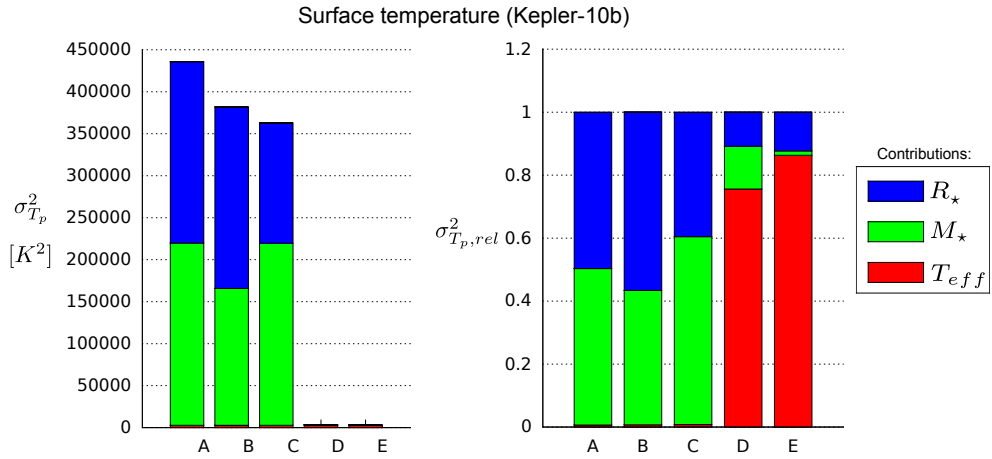


Figure B.9.: Variance of planetary surface temperature for all procedures of Kepler-10b.

## C. Tables and Figures for Kepler-22b

Table C.1.: Resulting parameters for Kepler-22b. Values below the single lines indicate the contributions to the variance of the corresponding parameter.

<b>Kepler-22</b>	<b>A</b>	<b>B</b>	<b>C</b>	<b>D</b>	<b>E</b>
$R_{\star} [R_{\odot}]$	9.79E-01	9.79E-01	9.79E-01	9.79E-01	9.79E-01
$\sigma_{R_{\star}} [R_{\odot}]$	5.70E-01	5.70E-01	3.63E-01	2.00E-02	1.96E-02
$\Delta\nu_{AS} [R_{\odot}^2]$	-	-	5.37E-05	-	-
$M_{\star,AS} [R_{\odot}^2]$	-	-	1.32E-01	-	-
$M_{\star} [M_{\odot}]$	9.70E-01	9.70E-01	9.70E-01	9.70E-01	9.70E-01
$\sigma_{M_{\star}} [M_{\odot}]$	1.32E+00	2.31E+00	1.32E+00	6.00E-02	1.94E-02
$R_{\star,AS} [M_{\odot}^2]$	1.71E+00	-	1.71E+00	-	-
$\log g_{\star,AS} [M_{\odot}^2]$	3.26E-02	-	3.26E-02	-	-
$\Delta\nu_{AS} [M_{\odot}^2]$	-	9.80E-04	-	-	-
$R_{\star,AS} [M_{\odot}^2]$	-	5.31E+00	-	-	-
$a [AU]$	8.49E-01	8.49E-01	8.49E-01	8.49E-01	8.49E-01
$\sigma_a [AU]$	3.85E-01	6.72E-01	3.85E-01	1.75E-02	5.66E-03
$\sigma_a/a$	4.53E-01	7.92E-01	4.53E-01	2.06E-02	6.67E-03
$P [AU^2]$	1.52E-11	1.52E-11	1.52E-11	1.52E-11	1.52E-11
$M_{\star} [AU^2]$	1.48E-01	4.52E-01	1.48E-01	3.06E-04	3.20E-05
$i [^{\circ}]$	8.98E+01	8.98E+01	8.98E+01	8.98E+01	8.98E+01
$\sigma_i [^{\circ}]$	1.79E-01	2.36E-01	1.44E-01	4.12E-02	4.09E-02
$\sigma_i/i$	1.99E-03	2.63E-03	1.61E-03	4.59E-04	4.56E-04
$\tilde{\sigma}_b^2 [^{\circ}^2]$	1.65E-03	1.65E-03	1.65E-03	1.65E-03	1.65E-03
$R_{\star} [^{\circ}^2]$	1.89E-02	1.89E-02	7.69E-03	2.33E-05	2.23E-05
$P [^{\circ}^2]$	1.18E-12	1.18E-12	1.18E-12	1.18E-12	1.18E-12
$M_{\star} [^{\circ}^2]$	1.15E-02	3.50E-02	1.15E-02	2.37E-05	2.48E-06
$M_p [M_{\oplus}]$	4.97E+01	4.97E+01	4.97E+01	4.97E+01	4.97E+01

Table C.1.: Resulting parameters for Kepler-22b. Values below the single lines indicate the contributions to the variance of the corresponding parameter.

<b>Kepler-22</b>	<b>A</b>	<b>B</b>	<b>C</b>	<b>D</b>	<b>E</b>
$\sigma_{M_p} [M_\oplus]$	8.75E+01	1.09E+02	8.75E+01	7.51E+01	1.02E+01
$\sigma_{M_p}/M_p$	1.76E+00	2.19E+00	1.76E+00	1.51E+00	2.05E-01
$K [M_\oplus^2]$	5.63E+03	5.63E+03	5.63E+03	5.63E+03	1.03E+02
$P [M_\oplus^2]$	1.31E-08	1.31E-08	1.31E-08	1.31E-08	1.31E-08
$M_\star [M_\oplus^2]$	2.03E+03	6.20E+03	2.03E+03	4.20E+00	4.39E-01
$R_\star [M_\oplus^2]$	2.42E-07	2.42E-07	9.83E-08	2.98E-10	2.85E-10
$b [M_\oplus^2]$	2.11E-08	2.11E-08	2.11E-08	2.11E-08	2.11E-08
$R_p [R_\oplus]$	2.37E+00	2.37E+00	2.37E+00	2.37E+00	2.37E+00
$\sigma_{R_p} [R_\oplus]$	1.39E+00	1.39E+00	8.90E-01	1.37E-01	1.37E-01
$\sigma_{R_p}/R_p$	5.85E-01	5.85E-01	3.75E-01	5.78E-02	5.76E-02
$R_\star [R_\oplus^2]$	1.91E+00	1.91E+00	7.75E-01	2.35E-03	2.25E-03
$M_\star [M_\oplus^2]$	1.64E-02	1.64E-02	1.64E-02	1.64E-02	1.64E-02
$\rho_p [\rho_\oplus]$	3.72E+00	3.72E+00	3.72E+00	3.72E+00	3.72E+00
$\sigma_{\rho_p} [\rho_\oplus]$	9.26E+00	1.04E+01	7.79E+00	5.66E+00	9.98E-01
$\sigma_{\rho_p}/\rho_p$	2.49E+00	2.81E+00	2.09E+00	1.52E+00	2.68E-01
$M_p [\rho_\oplus^2]$	4.30E+01	6.65E+01	4.30E+01	3.17E+01	5.80E-01
$R_p [\rho_\oplus^2]$	4.27E+01	4.27E+01	1.76E+01	4.17E-01	4.15E-01
$HZ_{\text{inner}} [AU]$	4.20E-01	4.20E-01	4.20E-01	4.20E-01	4.20E-01
$\sigma_{HZ_{\text{inner}}} [AU]$	2.45E-01	2.45E-01	1.56E-01	1.09E-02	1.07E-02
$\sigma_{HZ_{\text{inner}}}/HZ_{\text{inner}}$	5.82E-01	5.82E-01	3.72E-01	2.59E-02	2.56E-02
$R_\star [AU^2]$	5.98E-02	5.98E-02	2.43E-02	7.36E-05	7.05E-05
$T_{\text{eff}} [AU^2]$	4.49E-05	4.49E-05	4.49E-05	4.49E-05	4.49E-05
$HZ_{\text{outer}} [AU]$	7.84E-01	7.84E-01	7.84E-01	7.84E-01	7.84E-01
$\sigma_{HZ_{\text{outer}}} [AU]$	4.57E-01	4.57E-01	2.91E-01	2.03E-02	2.01E-02
$\sigma_{HZ_{\text{outer}}}/HZ_{\text{outer}}$	5.82E-01	5.82E-01	3.72E-01	2.59E-02	2.56E-02
$R_\star [AU^2]$	2.08E-01	2.08E-01	8.47E-02	2.57E-04	2.46E-04
$T_{\text{eff}} [AU^2]$	1.56E-04	1.56E-04	1.56E-04	1.56E-04	1.56E-04
$T_{\text{surface}} [K]$	2.62E+02	2.62E+02	2.62E+02	2.62E+02	2.62E+02
$\sigma_{T_{\text{surface}}} [K]$	9.68E+01	1.29E+02	7.69E+01	4.35E+00	3.47E+00
$\sigma_{T_{\text{surface}}}/T_{\text{surface}}$	3.69E-01	4.92E-01	2.93E-01	1.66E-02	1.32E-02

Table C.1.: Resulting parameters for Kepler-22b. Values below the single lines indicate the contributions to the variance of the corresponding parameter.

<b>Kepler-22</b>	<b>A</b>	<b>B</b>	<b>C</b>	<b>D</b>	<b>E</b>
$R_{\star} [K^2]$	5.84E+03	5.84E+03	2.37E+03	7.18E+00	6.89E+00
$T_{\text{eff}} [K^2]$	4.38E+00	4.38E+00	4.38E+00	4.38E+00	4.38E+00
$P [K^2]$	3.64E-07	3.64E-07	3.64E-07	3.64E-07	3.64E-07
$M_{\star} [K^2]$	3.54E+03	1.08E+04	3.54E+03	7.32E+00	7.65E-01

Table C.2.: Validation of the numerical methods for the Kepler-22 system. The last two rows are dimensionless. Reference values from Borucki et al. (2012).

Procedure		Value $x$	$\sigma_x$	$x - x_{\text{Ref.}}$	$\sigma_x/x$	$\frac{x-x_{\text{Ref.}}}{x_{\text{Ref.}}}$
$R_\star [R_\odot]$	Ref.	0.979	0.020	-	0.020	-
	A	1.140	0.570	0.161	0.500	0.164
	B	1.140	0.570	0.161	0.500	0.164
	C	1.080	0.363	0.161	0.500	0.164
	D	0.979	0.020	0.000	0.020	0.000
	E	0.979	0.020	0.101	0.337	0.103
$M_\star [M_\odot]$	Ref.	0.970	0.060	-	0.062	-
	A	1.306	1.319	0.336	0.020	0.347
	B	1.537	2.306	0.567	1.500	0.584
	C	1.306	1.319	0.336	0.020	0.347
	D	0.970	0.060	0.000	0.062	0.000
	E	0.970	0.019	0.000	1.009	0.000
$a_p [R_\star]$	Ref.	186.400	1.600	-	0.009	-
	A	176.684	106.485	-9.716	0.062	-0.052
	B	186.521	131.896	0.121	0.707	0.001
	C	186.521	88.771	0.121	0.020	0.001
	D	186.304	5.408	-0.096	0.029	-0.001
	E	186.304	3.928	-0.096	0.476	-0.001
$i_p [^\circ]$	Ref.	89.764	0.042	-	0.000	-
	A	89.751	0.156	-0.013	0.029	0.000
	B	89.764	0.172	0.000	0.002	0.000
	C	89.764	0.119	0.000	0.021	0.000
	D	89.764	0.041	0.000	0.000	0.000
	E	89.764	0.041	0.000	0.001	0.000
$R_p [R_\oplus]$	Ref.	2.380	0.130	-	0.055	-
	A	2.762	1.389	0.382	0.000	0.160
	B	2.762	1.389	0.382	0.503	0.160
	C	2.616	0.892	0.236	0.000	0.099
	D	2.372	0.137	-0.008	0.058	-0.003
	E	2.372	0.137	-0.008	0.341	-0.003
$M_p [M_\oplus]$	Ref.	36.000	0.000	-	0.000	-
	A	60.600	100.195	24.600	0.058	0.683
	B	67.536	122.330	31.536	1.811	0.876
	C	60.600	100.195	24.600	0.058	0.683
	D	49.691	75.072	13.691	1.511	0.380
	E	49.691	10.163	13.691	1.653	0.380



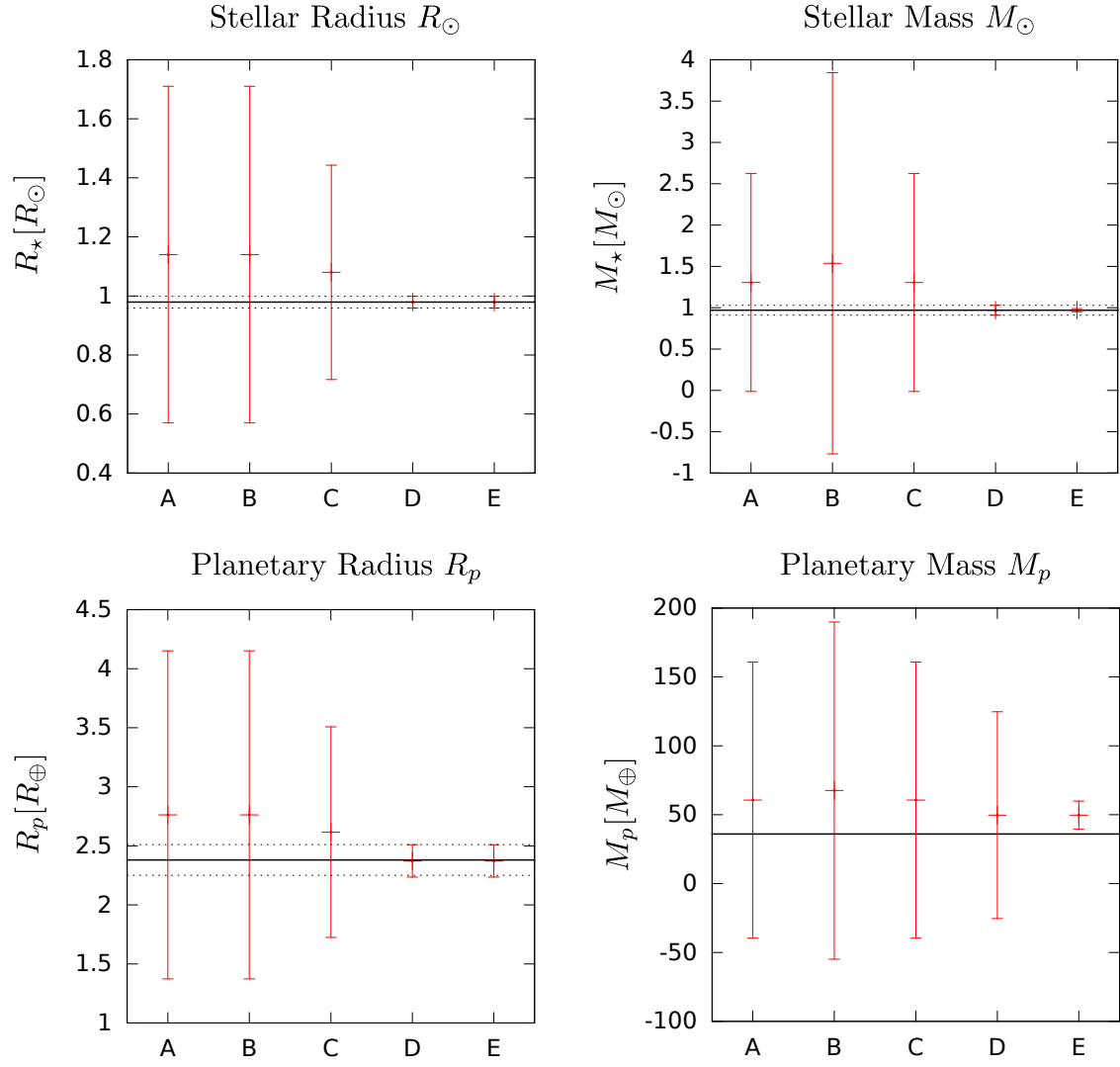


Figure C.1.: Validation of the numerical methods for Kepler-22. For a description see Figure 5.1. Again for the error of planetary mass there does not exist a specific value. Reference values from Borucki et al. (2012).

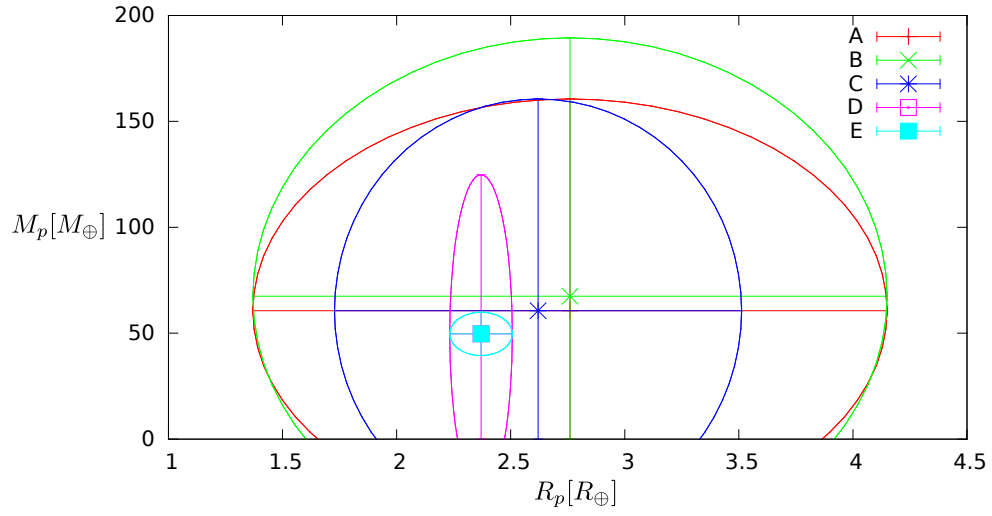


Figure C.2.: Planetary radius vs. mass for all procedures of Kepler-22b with corresponding areas of 1 standard deviation (ellipses).

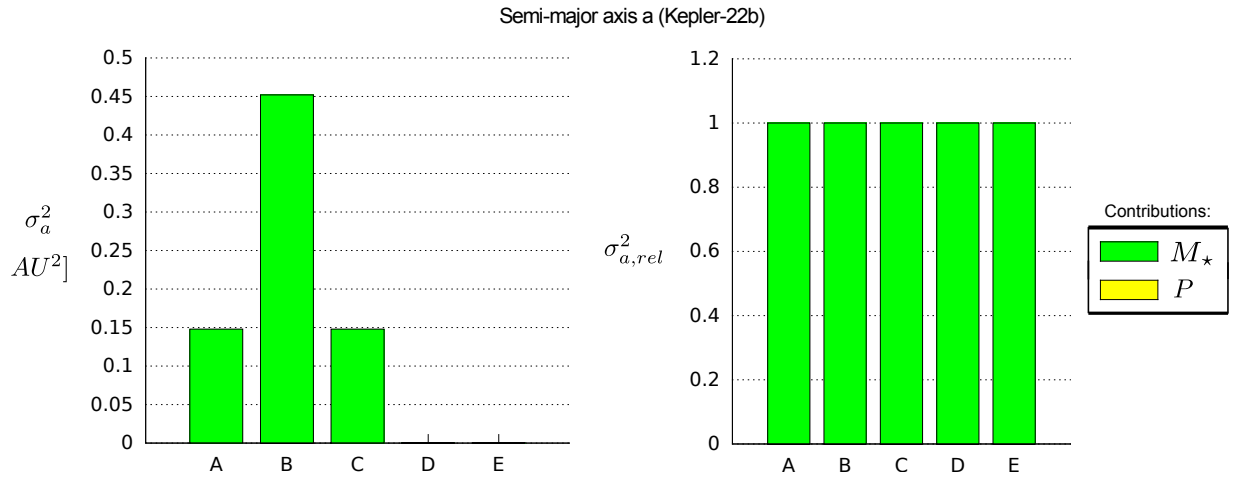


Figure C.3.: Variance of  $a$  for all procedures of Kepler-22b.

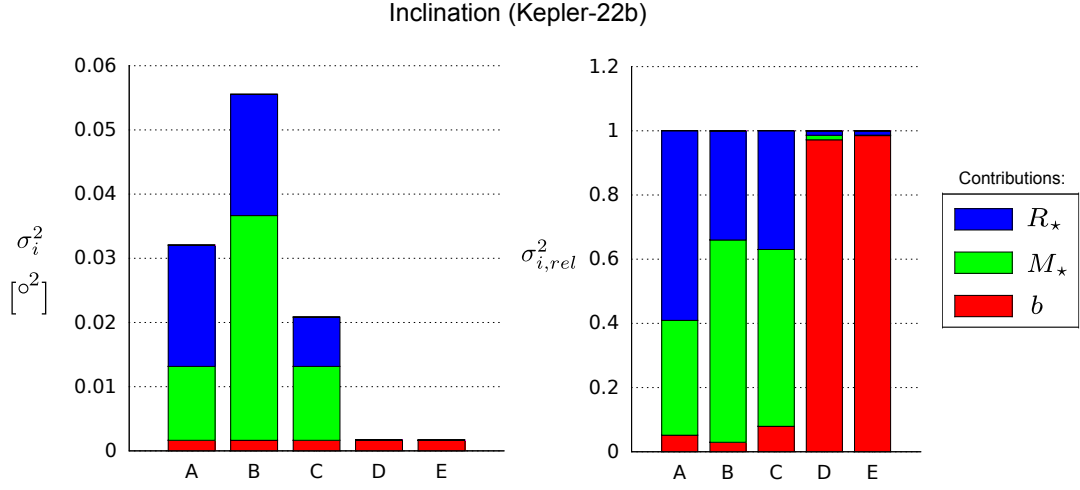


Figure C.4.: Variance of  $i$  for all procedures of Kepler-22b.

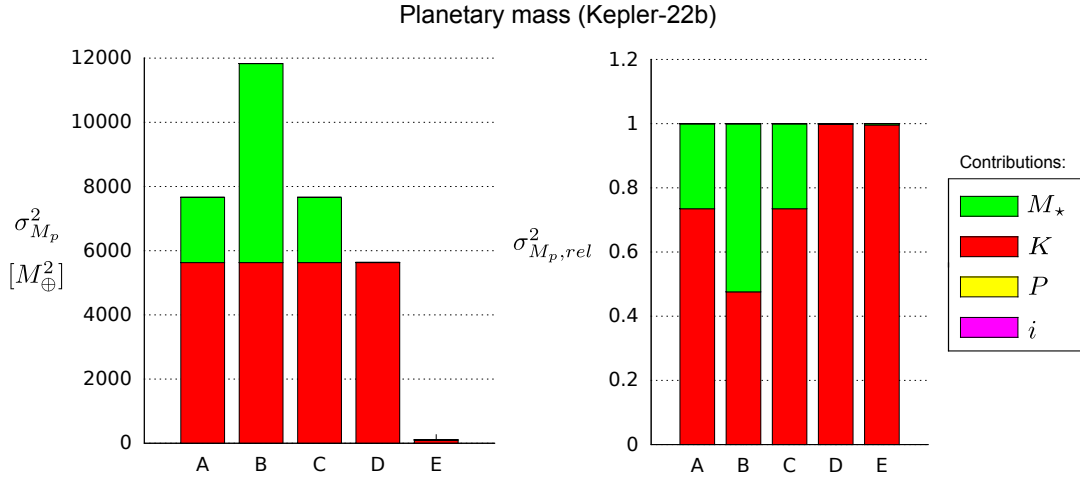


Figure C.5.: Variance of  $M_p$  for all procedures of Kepler-22b.

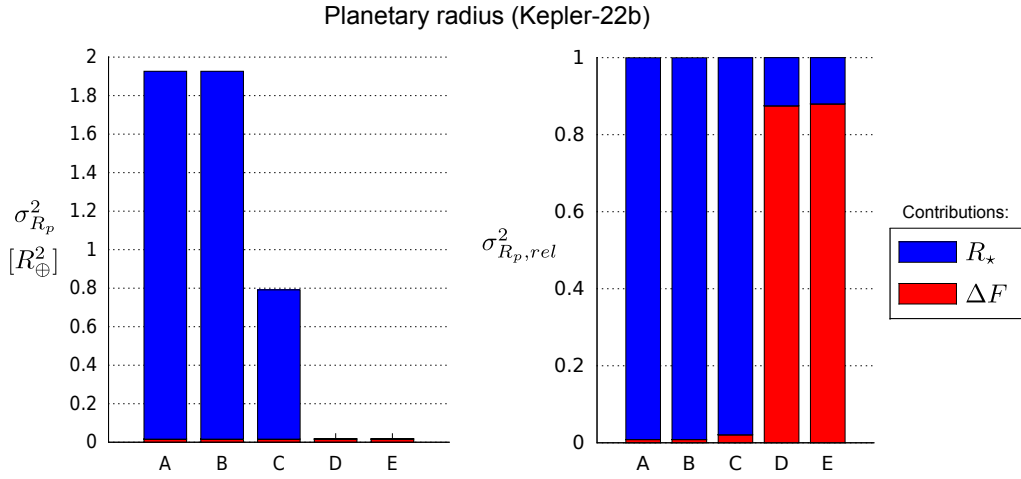


Figure C.6.: Variance of  $R_p$  for all procedures of Kepler-22b.

### C. Tables and Figures for Kepler-22b

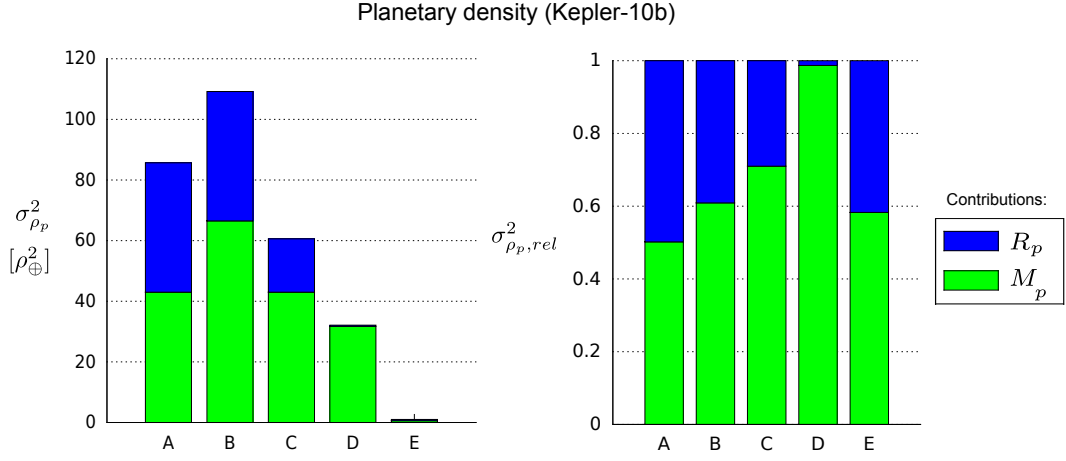


Figure C.7.: Variance of  $\rho_p$  for all procedures of Kepler-22b.

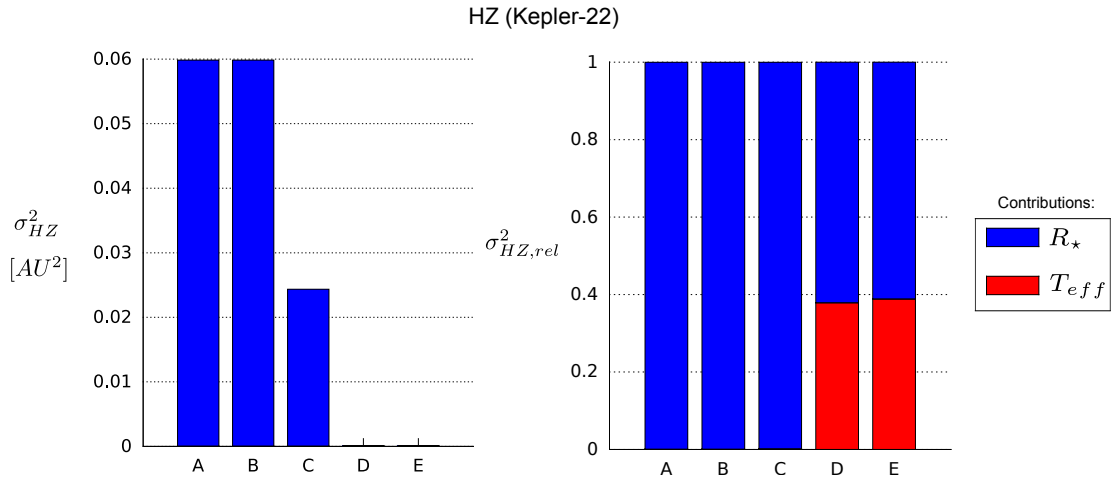


Figure C.8.: Variance of the boundaries of the HZ for all procedures of Kepler-22b.

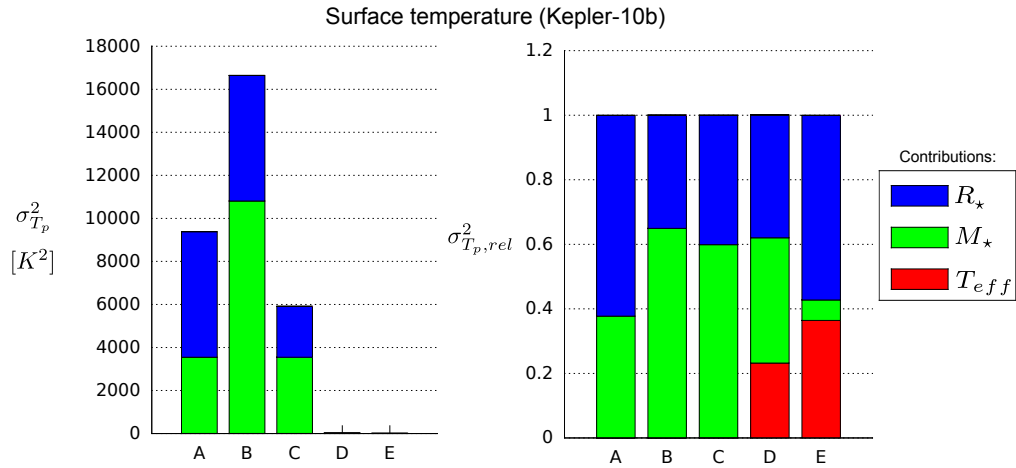


Figure C.9.: Variance of planetary surface temperature for all procedures of Kepler-22b.

# Bibliography

- AERTS, C., CHRISTENSEN-DALSGAARD, J. & KURTZ, D. W. (2010) *Asteroseismology*. Springer Science+Business Media B.V.
- APPOURCHAUX, T., BELKACEM, K., BROOMHALL, A.-M., CHAPLIN, W. J., GOUGH, D. O., HOUDEK, G., PROVOST, J., BAUDIN, F. ET AL. (2010) The quest for the solar g modes. *A&A Rev.*, **18**, 197–277.
- BAILER-JONES, C. A. L. (2002) Determination of Stellar Parameters with GAIA. *Ap&SS*, **280**, 21–29.
- BATALHA, N. M., BORUCKI, W. J., BRYSON, S. T., BUCHHAVE, L. A., CALDWELL, D. A., CHRISTENSEN-DALSGAARD, J., CIARDI, D., DUNHAM, E. W. ET AL. (2011) Kepler’s First Rocky Planet: Kepler-10b. *ApJ*, **729**, 27.
- BESSELL, M. S. (2007) Bolometric corrections to Hipparcos Hp magnitudes and UBVRI colours. <http://msowww.anu.edu.au/~bessell/>, retrieved 2012-06-30.
- BESSELL, M. S. (2012) Bolometric corrections to Hipparcos Hp magnitudes and UBVRI colors. <http://www.mso.anu.edu.au/~bessell/>, retrieved 2012-07-06.
- BORUCKI, W. J., KOCH, D., BASRI, G., Batalha, N., BROWN, T., CALDWELL, D., CALDWELL, J., CHRISTENSEN-DALSGAARD, J. ET AL. (2010) Kepler Planet-Detection Mission: Introduction and First Results. *Science*, **327**, 977–.
- BORUCKI, W. J., KOCH, D. G., Batalha, N., BRYSON, S. T., ROWE, J., FRESSIN, F., TORRES, G., CALDWELL, D. A. ET AL. (2012) Kepler-22b: A 2.4 Earth-radius Planet in the Habitable Zone of a Sun-like Star. *ApJ*, **745**, 120.
- CATALA, C. (2009) PLATO: PLANetary Transits and Oscillations of stars. *Communications in Asteroseismology*, **158**, 330.

- CATALA, C. E. A. (2011) PLATO Red Book - Definition Study Report. <http://sci.esa.int/science-e/www/object/index.cfm?fobjectid=48984>, retrieved 2012-06-26.
- CHRISTENSEN-DALSGAARD, J. (1993) On the Asteroseismic HR Diagram. In *GONG 1992. Seismic Investigation of the Sun and Stars*, edited by T. M. Brown, vol. 42 of *Astronomical Society of the Pacific Conference Series*.
- CHRISTENSEN-DALSGAARD, J. (2008) Helio- and asteroseismology. In *IAU Symposium*, edited by L. Deng & K. L. Chan, vol. 252 of *IAU Symposium*.
- CHRISTENSEN-DALSGAARD, J. & THOMPSON, M. J. (2011) Stellar hydrodynamics caught in the act: Asteroseismology with CoRoT and Kepler. In *IAU Symposium*, edited by N. H. Brummell, A. S. Brun, M. S. Miesch & Y. Ponty, vol. 271 of *IAU Symposium*.
- COX, J. P. (1980) *Theory of stellar pulsation*. Princeton University Press.
- CUMMING, A., MARCY, G. W. & BUTLER, R. P. (1999) The Lick Planet Search: Detectability and Mass Thresholds. *ApJ*, **526**, 890–915.
- CUNHA, M. S., AERTS, C., CHRISTENSEN-DALSGAARD, J., BAGLIN, A., BIGOT, L., BROWN, T. M., CATALA, C., CREEVEY, O. L. ET AL. (2007) Asteroseismology and interferometry. *A&A Rev.*, **14**, 217–360.
- EXELIS VISUAL INFORMATION SOLUTIONS (2012) Interactive Data Language. <http://www.exelisvis.com>, retrieved 2012-07-05.
- FLOWER, P. J. (1996) Transformations from Theoretical Hertzsprung-Russell Diagrams to Color-Magnitude Diagrams: Effective Temperatures, B-V Colors, and Bolometric Corrections. *ApJ*, **469**, 355.
- GIZON, L. & SOLANKI, S. K. (2003) Determining the Inclination of the Rotation Axis of a Sun-like Star. *ApJ*, **589**, 1009–1019.
- GOUGH, D. O. (1986) EBK Quantization of Stellar Waves. In *Hydrodynamic and Magnetodynamic Problems in the Sun and Stars*, edited by Y. Osaki.
- GRAY, R. (2000) *Effective Temperature Scale and Bolometric Corrections*.
- HASWELL, C. A. (2010) *Transiting Exoplanets*. Cambridge University Press.

- HØG, E. (2000) *Tycho Star Catalogs: The 2.5 Million Brightest Stars*.
- HOWELL, S. B., ROWE, J. F., BRYSON, S. T., QUINN, S. N., MARCY, G. W., ISAACSON, H., CIARDI, D. R., CHAPLIN, W. J. ET AL. (2012) Kepler-21b: A  $1.6 R_{Earth}$  Planet Transiting the Bright Oscillating F Subgiant Star HD 179070. *ApJ*, **746**, 123.
- KEPLER MISSION TEAM (2009) Kepler Input Catalog (Kepler Mission Team, 2009). *VizieR Online Data Catalog*, **5133**, 0.
- KOVTYUKH, V. V., SOUBIRAN, C., BELIK, S. I. & GORLOVA, N. I. (2003) High precision effective temperatures for 181 F-K dwarfs from line-depth ratios. *A&A*, **411**, 559–564.
- LÉGER, A., ROUAN, D., SCHNEIDER, J., BARGE, P., FRIDLUND, M., SAMUEL, B., OLLIVIER, M., GUENTHER, E. ET AL. (2009) Transiting exoplanets from the CoRoT space mission. VIII. CoRoT-7b: the first super-Earth with measured radius. *A&A*, **506**, 287–302.
- LINDEGREN, L. (2009) Gaia: Astrometric Performance and Current Status of the Project. In *IAU Symposium #261, American Astronomical Society*, vol. 261.
- MAYOR, M. & QUELOZ, D. (1995) A Jupiter-mass companion to a solar-type star. *Nature*, **378**, 355–359.
- MONTEIRO, M. J. P. F. G., CHRISTENSEN-DALSGAARD, J. & THOMPSON, M. J. (2002) Asteroseismic inference for solar-type stars. In *Stellar Structure and Habitable Planet Finding*, edited by B. Battick, F. Favata, I. W. Roxburgh & D. Galadi, vol. 485 of *ESA Special Publication*.
- NAGAOKA, H. & MISHIMA, T. (1923) A Combination of a Concave Grating with a Lummer-Gehrcke Plate or an Echelon Grating for Examining Fine Structure of Spectral Lines. *ApJ*, **57**, 92.
- NASA (2012) Kepler - A Search for Habitable Planets. <http://kepler.nasa.gov/>, retrieved 2012-07-04.
- PERRYMAN, M. (2011) *The Exoplanet Handbook*. Cambridge University Press.

## Bibliography

- PERRYMAN, M. A. C. & ESA (eds.) (1997) *The HIPPARCOS and TYCHO catalogues. Astrometric and photometric star catalogues derived from the ESA HIPPARCOS Space Astrometry Mission*, vol. 1200 of *ESA Special Publication*.
- SCHNEIDER, J. (2012) The Extrasolar Planets Encyclopedia - Interactive Extrasolar Planets Catalog. <http://exoplanet.eu/catalog.php>, retrieved 2012-07-10.
- STAHN, T. (2011) Analysis of time series of solar-like oscillations – Applications to the Sun and HD 52265. Ph.D. thesis.
- STSCI/NASA (2008) Measuring trigonometric parallax. <http://www.stsci.edu>, retrieved 2012-07-06.
- TASSOUL, M. (1980) Asymptotic approximations for stellar nonradial pulsations. *ApJS*, **43**, 469–490.
- UNNO, W., OSAKI, Y., ANDO, H., SAIO, H. & SHIBAHASHI, H. (1989) *Nonradial oscillations of stars*.
- VALENTI, J. A. & FISCHER, D. A. (2005) Spectroscopic Properties of Cool Stars (SPOCS). I. 1040 F, G, and K Dwarfs from Keck, Lick, and AAT Planet Search Programs. *ApJS*, **159**, 141–166.
- VAN LEEUWEN, F. (2007) Validation of the new Hipparcos reduction. *A&A*, **474**, 653–664.
- VERNER, G. A., CHAPLIN, W. J., BASU, S., BROWN, T. M., HEKKER, S., HUBER, D., KAROFF, C., MATHUR, S. ET AL. (2011) Verification of the Kepler Input Catalog from Asteroseismology of Solar-type Stars. *ApJ*, **738**, L28.
- VOGT, S. S., MARCY, G. W., BUTLER, R. P. & APPS, K. (2000) Six New Planets from the Keck Precision Velocity Survey. *ApJ*, **536**, 902–914.



# Danksagung

At first I would like to thank Prof. Dr. Laurent Gizon to get the chance to do this thesis under his supervision and in his workgroup at the university and for the frequent meetings which helped me a lot in approaching the goals of this work. Investigating extrasolar planets and learning more about exciting new research areas like the application of asteroseismic methods on exoplanetary systems was really amazing and I got many new insights in scientific processes. The work on this thesis encouraged me to aim for a scientific career.

I also want to thank Prof. Dr. Stefan Dreizler for acting as a second referee of this thesis; Dr. Thorsten Stahn and Dr. João Marques for their continuous assistance and hints and their willingness to deal even with trivial problems; and my fellow students Andre Lamert and Alexander Schmelev for helping one another with our bachelor theses.

Last but not least I want to thank my parents Margit and Fred Lichtenberg and my girlfriend Lola-Sophia Krug for there permanent support and love, which help me a lot to succeed in daily work.

**Erklärung** nach §13(8) der Prüfungsordnung für den Bachelor-Studiengang Physik und den Master-Studiengang Physik an der Universität Göttingen:

Hiermit erkläre ich, dass ich diese Abschlussarbeit selbständig verfasst habe, keine anderen als die angegebenen Quellen und Hilfsmittel benutzt habe und alle Stellen, die wörtlich oder sinngemäß aus veröffentlichten Schriften entnommen wurden, als solche kenntlich gemacht habe.

Darüberhinaus erkläre ich, dass diese Abschlussarbeit nicht, auch nicht auszugsweise, im Rahmen einer nichtbestanden Prüfung an dieser oder einer anderen Hochschule eingereicht wurde.

Göttingen, den August 6, 2012

(Tim Lichtenberg)